National Technical University of Athens
School of Mechanical Engineering Parallel
CFD & Optimization Unit

Adjoint shape optimization of two tandem hydrofoils

Master's Thesis
Joint Postgraduate Program "Computational Mechanics"
by

Anastasios Argyriou

Supervisor:
Prof. K.G. Giannakoglou, School of Mech. Eng., NTUA

February 2026

Abstract

This Master's Thesis presents a CFD analysis and shape optimization study of two tandem hydrofoils, focusing on the influence of design and operational parameters by considering various objective functions, such as drag and lift, subject to geometric constraints. The flow simulations are all conducted using the open-source CFD software OpenFOAM, employing its solvers and meshing tools for geometry generation and solution of the Navier–Stokes equations.

Shape optimization is carried out using the adjointOptimisationFoam library, programmed and made publicly available by the PCOpt/NTUA, applying the continuous adjoint method to compute sensitivity derivatives and guide shape modifications. The initial configuration consists of two NACA 4412 hydrofoils, the one behind the other. Parametric studies are performed across a range of inter-foil distances and common position angles, while the infinite flow angle is kept steadily at 0° and the common position angle at 9° for multiple optimization scenarios.

Each optimization case explored different combinations of objective functions—targeting either lift, drag, or both applied to each hydrofoil individually or as a common computed coefficient. The decision to keep common or distinct geometries for the front and rear hydrofoils, affected both the optimization targets and the calculated sensitivities of each scenario. The results demonstrate that adjoint-based optimization can significantly improve hydrodynamic performance, enabling the design of customized foil geometries with enhanced lift-to-drag characteristics.

Tandem hydrofoils are utilized in the maritime industry at high speed vessels that operate with their hull lifted out of the water in their sailing velocity. This allows them to achieve better speed-resistance ratio and improve their overall efficiency. In this case, the shape optimization of each hydrofoil can allow the vessel designer to allocate the weight of the hull on each foil, while he maintains the desired lift for operation.

Περίληψη

Η Μεταπτυχιακή αυτή εργασία παρουσιάζει μια ανάλυση υπολογιστικής ρευστοδυναμικής και μελέτη βελτιστοποίησης σχήματος δύο διαδοχικών υδροτομών, με έμφαση στην επίδραση παραμέτρων σχεδιασμού και λειτουργίας υπό διάφορες αντικειμενικές συναρτήσεις, όπως η οπισθέλκουσα και η άνωση, λαμβάνοντας υπόψη γεωμετρικούς περιορισμούς. Όλες οι προσομοιώσεις ροής πραγματοποιούνται με το λογισμικό ανοιχτού κώδικα OpenFOAM, χρησιμοποιώντας τους επιλύτες και τα εργαλεία δημιουργίας πλέγματος για τη γεωμετρία και την επίλυση των εξισώσεων Navier–Stokes.

Η βελτιστοποίηση σχήματος εκτελείται με τη χρήση της βιβλιοθήκης adjointOptimisationFoam, η οποία έχει αναπτυχθεί και είναι ανοιχτή προς όλους από την μονάδα PCOpt/NTUA, εφαρμόζοντας τη συνεχή συζυγή μέθοδο για τον υπολογισμό πεδίων ευαισθησίας και την καθοδήγηση τροποποιήσεων στο σχήμα. Η αρχική διάταξη αποτελείται από δύο υδροτομές τύπου NACA 4412. Πραγματοποιούνται παραμετρικές μελέτες για διάφορες αποστάσεις μεταξύ των υδροτομών και κοινές γωνίες τοποθέτησης, ενώ η γωνία της επάπειρου ροής διατηρείται σταθερή στις 0°, με τελική επιλογή γωνίας τοποθέτησης 9° για πολλαπλά σενάρια βελτιστοποίησης.

Κάθε περίπτωση βελτιστοποίησης εξετάζει διαφορετικούς συνδυασμούς αντικειμενικών συναρτήσεων—στοχεύοντας είτε στην άνωση, είτε στην αντίσταση, είτε και στα δύο σε κάθε υδροτομή ξεχωριστά ή ως κοινοί συντελεστές και για τις δύο. Αυτό έχει ως αποτέλεσμα είτε κοινές είτε διαφορετικές γεωμετρίες για την εμπρόσθια και την οπίσθια υδροτομή, ανάλογα με τους στόχους βελτιστοποίησης και τις συναρτήσεις ευαισθησίας που υπολογίστηκαν. Τα αποτελέσματα δείχνουν ότι η βελτιστοποίηση μέσω της συζυγούς μεθόδου μπορεί να βελτιώσει σημαντικά τις υδροδυναμικές επιδόσεις, επιτρέποντας τον σχεδιασμό γεωμετριών με βελτιωμένο λόγο άνωσης προς αντίσταση ειδικά διαμορφωμένο στην κάθε εφαρμογή.

Η πραγματική εφαρμογή των διαδοχικών υδροπτερύγων συναντάται στη ναυπηγική βιομηχανία, σε σκάφη υψηλών ταχυτήτων που κινούνται με το κύτος ανυψωμένο εκτός νερού κατά την ταχύτητα πλεύσης τους. Με αυτόν τον τρόπο, επιτυγχάνεται καλύτερος λόγος ταχύτητας-αντίστασης και βελτιωμένη συνο-

λική απόδοση. Σε αυτήν την περίπτωση, η βελτιστοποίηση σχήματος των υδροπτερύγων δίνει τη δυνατότητα στον σχεδιαστή να κατανείμει το βάρος του κύτους σε αυτές, διατηρώντας παράλληλα την επιθυμητή άνωση για την ομαλή λειτουργία.

Acronyms

CFD Computational Fluid Mechanics

L edge-to-edge distance

NTUA National Technical University of Athens

PCopt Parallel CFD & Optimization unit

RANS Reynolds-averaged Navier–Stokes

ShpO Shape Optimization

Contents

Chapter 1

Introduction

1.1 Tandem Hydrofoils

Hydrofoils are widely utilized in high-performance marine vessels to reduce hydrodynamic drag and enable higher speeds compared to conventional displacement hulls [1]. The fundamental operating principle relies on the generation of lift by submerged foils, which elevates the vessel's hull above the water surface. Once the hull is lifted out of the water, the vessel experiences significantly reduced viscous and form drag due to the lower density and viscosity of air compared to water, thereby improving overall efficiency and attainable speed. At the same time, although the hydrofoils consist a part of the hull, they remain constantly within the water region as a fundamental principle of their operation.

In configurations employing multiple hydrofoils—particularly tandem arrangements— (e.g., Soviet made Hydrofoil craft Raketa [2],Olympia, Red Sormovo etc. shown at figure 1.1 & 1.2) the flow dynamics become increasingly complex due to the mutual hydrodynamic interactions between the foils. The leading (fore) hydrofoil generates a wake characterized by reduced pressure, increased turbulence, and velocity deficits, which influences the flow environment encountered by the trailing (aft) hydrofoil [3]. In general, this results in overall reduced lift and increased drag for the configuration, harming the vessel's operational efficiency(e.g. fuel consumption or cargo carried).

The aft hydrofoil, operating in this disturbed wake region, typically experiences a reduction in effective inflow velocity. This leads to a corresponding decrease in lift generation, potentially impacting stability and control [4]. As a result, in tandem hydrofoil systems, lift is not evenly distributed: the fore hydrofoil may exhibit increased lift due to cleaner upstream flow, while

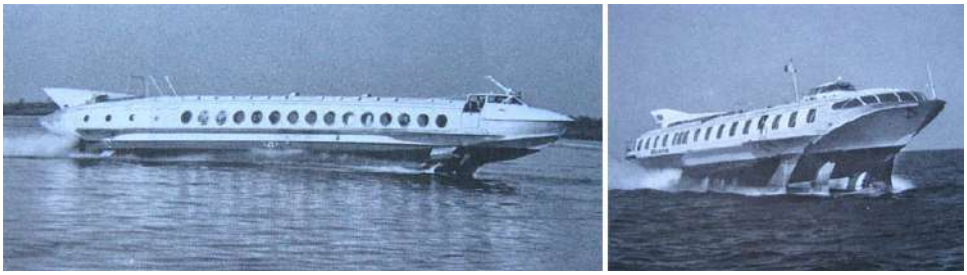

Figure 1.1: The soviet made hydrofoil vessels "Raketas" in operation [5].

Figure 1.2: The soviet made hydrofoil vessels "Raketas" in operation [5].

the aft foil tends to generate less lift. In terms of drag, the fore hydrofoil often benefits from lower resistance due to undisturbed flow, whereas the aft foil can suffer increased drag due to higher turbulence intensity and flow separation in the wake region.

A particularly notable phenomenon is the possibility of negative drag occurring at the fore hydrofoil under certain geometric configurations or operating conditions [6].

The above indicates that during the designing phase of a hydrofoil vessel, the designer has to take into consideration of the interaction before the fore-aft foil and modify them to achieve the required forces for operation [7]. This MSc thesis is studying this interaction and performs several optimization runs in different setups that can assist understanding the flow our two horizontally tandem hydrofoils.

In this thesis, all simulations and analyses are based on a tandem hydrofoil configuration with two NACA4412 foils, where the vertical position of both foils is held constant—they are aligned at the same depth below the water surface and free-surface effects are neglected.

Figure 1.3: Two tandem hydrofoils and the distance between them in real scale.

The main variables to be decided and applied prior the ShpO and the tandem foil performance evaluation are:

- The longitudinal distance between the two hydrofoils which will be parametrically studied, and
- The common position angle for both foils that will be examined at two values, namely either at 0 or 9 degrees.

while the infinite flow angle is fixed at 0 degrees.

These parameters are systematically varied in computational simulations to analyze their influence on hydrodynamic performance, including lift and drag coefficients, flow separation, and potential cavitation. The results are presented in subsequent chapters, where force coefficients are compared across multiple configurations to identify optimal spacing and position angles for performance and efficiency.

1.2 Shape Optimization

The process of designing an optimal geometry based on an objective function is a complex engineering challenge. Traditional design methodologies often rely on an iterative approach, combining empirical rules, analytical models, and the engineer's intuition. This process typically involves generating a baseline geometry, evaluating its performance through experimental testing or computational simulation, and then manually modifying its shape based on the results. While this approach can yield functional designs, it is inherently limited. It is time-consuming, computationally & financially expensive, and heavily dependent on the designer's experience. Crucially, it offers no guarantee of convergence towards a truly optimal solution, often resulting in designs that are merely satisfactory rather than optimal.

ShpO presents a formal and systematic methodology to overcome these limitations. It is a branch of computational design that employs mathematical algorithms to automate the search for the best possible geometry within a predefined design space. The core of this methodology can be defined as an iterative numerical procedure that seeks to minimize (or maximize) an *objective function* $F(\vec{b})$, which quantifies the performance of the system (e.g., minimize drag coefficient C_D, maximize lift-to-drag ratio L/D), by systematically adjusting a set of *design variables* $\vec{b}_n = (b_1, b_2, ..., b_n)$ that parameterize the geometry. This optimization is performed while satisfying a set of *constraints* $g(\vec{b})$ (e.g., a fixed lift coefficient C_L, minimum thickness or volume requirements, structural limits etc.).

The general optimization problem can be formally stated as:

$$\begin{aligned} \underset{b}{\text{minimize}} \quad & F(\vec{b}) \\ \text{subject to} \quad & g_i(\vec{b}) \leq a \text{ or } g_i(\vec{b}) = a \text{ or } g_i(\vec{b}) \geq a, i = 1, \ldots, m \\ & \vec{b}^L \leq \vec{b} \leq \vec{b}^U \end{aligned} \tag{1.1}$$

where $a \in \mathbb{R}$, $\vec{b}^L$ and $\vec{b}^U$ represent the lower and upper bounds of the design variables respectively, and if they exist which is not mandatory, then they limit the feasible design space of the optimization process. We assume that $g(\vec{b})$ should be below zero.

A critical component of any ShpO framework is the *parameterization* scheme, which defines how the design variables $\vec{b}$ control the geometry. An effective parameterization must provide sufficient flexibility to explore a wide range of shapes while maintaining geometric validity and practicality. Common techniques include using spline control points, polynomial functions, or basis vectors from modal analyses.

The optimization loop is executed by a dedicated numerical algorithm, which guides the search through the design space. Algorithms can be broadly categorized into *gradient-based* methods and *gradient-free* (or stochastic) methods [8]. Gradient-based methods (e.g.,steepest descent, Newton, Quasi-Newton, adjoint-based optimization [9]) utilize gradient information of the objective function and constraints to rapidly converge to a local optimum. They can be computationally efficient if the sensitivities are computed accurate and combined with a robust gradient calculation method (e.g. adjoint [10]) . In contrast, gradient-free methods (e.g., Evolutionary Algorithms, etc.) do not require gradient information and are better at exploring the global design space, though they typically require a much larger number of function evaluations (CFD runs).

The evaluation of the objective function and constraints, often referred to as the *analysis*, is performed by a high-fidelity Computational Fluid Dynamics (CFD) solver. The solver provides the necessary performance metrics (e.g., force coefficients, pressure distributions) for a given geometry. The integration of the optimization algorithm with the CFD solver is therefore fundamental, creating an automated workflow where the geometry is modified, the mesh is updated, the flow is simulated, and the results are fed back to the optimizer until a convergence criterion is met.

1.3 AdjointFoam Library and openFoam

OpenFOAM [11] is an open-source, C++-based computational fluid dynamics (CFD) toolbox designed for solving a wide range of fluid mechanics problems. It has grown into one of the most widely used CFD platforms in both academia and industry, due to its flexibility, transparency, and powerful solvers.

OpenFOAM provides a rich set of solvers capable of handling various physical phenomena, including incompressible and compressible fluid flows (e.g., via simpleFoam, pimpleFoam, rhoPimpleFoam etc; steady or unsteady) along with a variety of turbulence models.

At its core, OpenFOAM is a pressure-based algorithm which uses the finite volume method (FVM) to discretize and solve the governing equations (e.g., Navier–Stokes equations), making it highly adaptable for custom physics and numerical schemes.

A distinctive advantage of OpenFOAM is its modular architecture, which allows users to combine solvers, utilities, and libraries, or even develop their own modules. This extensibility is particularly valuable in research contexts where custom setups or novel methods are required.

Accurate CFD simulations depend heavily on mesh quality and OpenFOAM offers both structured and unstructured meshing utilities:

- blockMesh [12]: A tool for creating structured, hexahedral meshes using a dictionary-based approach. It is simple and efficient for geometrically regular domains.
- snappyHexMesh [13]: A powerful tool for generating body-fitted unstructured meshes. It allows for surface snapping and layer addition, making it suitable for complex geometries such as hydrofoil profiles.

Mesh generation can be integrated seamlessly into simulation workflows, with additional support for refinement zones, boundary layer control, and automated mesh quality checks. The subject thesis utilize both of the above tools, blockMesh for the background mesh generation and snappyHexMesh to cut-in the hydrofoils.

One of the main tools used in this thesis is the adjointFoamOptimization library within OpenFOAM, programmed and made publicly available by the PCopt/NTUA, typically accessed through the adjointOptimisationFoam solver [14]. This library enables gradient-based ShpO using the continuous adjoint method.

The adjoint method involves solving an additional set of equations allowing for the computation of the sensitivities of one or more objective functions (e.g., drag, lift, or pressure drop) with respect to various design variables. The method is computationally efficient because it provides gradients of a single function with respect to all design variables using only one adjoint solution, regardless of the number of design variables, at a cost that is more or less similar to that of the primal equation.

Main features of the adjointOptimisationFoam framework include:

- Support for incompressible turbulent flows (such as Reynolds-averaged Navier–Stokes) models with the k–ω SST [15], as used within this MSc Thesis or Spalart-Almarras)
- Capability to define and calculate various objective functions, such as drag or lift in forces.
- Availability of various gradient optimization methods to update the design variables.
- Integration with mesh deformation tools for iterative geometry updates.

This makes it particularly suitable for automated ShpO of marine components, such as hydrofoils, where fine-tuning the geometry can significantly impact hydrodynamic performance.

Chapter 2

Background

2.1 Grid generation

As already mentioned at Chapter 1, the generated grids used in this MSc thesis are results from the synergistic use of blockMesh and snappyHexMesh, from openFoam's library. The first one is utilized to create the initial structured background mesh, much finer close to the hydrofoils or their wake region, which will be the foundation of the final grid. The second tool is utilized to implement the surfaces (e.g. hydrofoils in STL file form) in the first grid and then, apply all the required refinement levels and boundary layers stretching.

Although the initial generated mesh is 3D, ensuring compliance to a fundamental requirement of the snappyHexMesh, the final mesh that is being used in the computations is 3D, having one cell at third (z) direction. While the above seems to easily vanish any issues that may occur from 2D applications relying at 3D meshing tools, the initial 3D mesh requirements in cells (prior extracting the third dimension at one cell width) are significant larger than the 2D version, especially if several refinement levels are utilized considering that all three dimensions are becoming finer. The drawbacks of the above are the extra time and resources required to generate each grid and the possible constraints set by the researcher's system configuration, in number of memory and total cells supported.

The overall dimensions of the grids used in this thesis can be seen in the 2.1.

The zero point (0,0) is the trailing edge of the fore hydrofoil and the distances are chosen while following the general CFD guidelines, based on the length of the studied item which in this case is a foil with unit chord (C).

For the sake of consistency and due to limitations in the numbers of cells

Axis	x	y
Min	-5	-3
Max	15	3

Table 2.1: Size of computational domain.

(all computations were performed on personal computers), the grid bounding dimensions have been kept the same for both single foil and tandem mode system configurations.

2.2 The Steady Incompressible RANS Equations

In industrial engineering applications such as internal or external flows around vehicles, turbulence plays a significant role and must accurately be modeled. The RANS equations are widely employed for such purposes. Originally proposed by Reynolds in 1895, this approach decomposes each flow variable into a mean and a fluctuating component. By substituting this decomposition into the Navier-Stokes equations and performing a time-averaging operation, the RANS equations are obtained. These equations govern the mean quantities, while the effects of the fluctuations appear as additional terms that require modeling. The equations consist of the mass and momentum conservation equations:

$$R^p = -\frac{\partial v_j}{\partial x_j} = 0 \tag{2.1}$$

$$R_i^v = v_j \frac{\partial v_i}{\partial x_j} - \frac{\partial \tau_{ij}}{\partial x_j} + \frac{\partial p}{\partial x_i} = 0, \quad i = 1, 2(, 3) \tag{2.2}$$

where u_i are the averaged velocity components, p the pressure divided by the density (assumed constant for incompressible flow), ρ is the fluid density

The RANS equations retain the same mathematical structure of the instantaneous Navier-Stokes equations, but involve time-averaged flow quantities. In particular, the influence of turbulence is modeled by introducing the turbulent (or eddy) viscosity ν_t, which is added to the molecular viscosity ν. Following Boussinesq's hypothesis, the turbulent stresses are modeled analogously to viscous stresses, resulting in a modified stress tensor:

$$\tau_{ij} = (\nu + \nu_t) \left[\left(\frac{\partial v_i}{\partial x_j} + \frac{\partial v_j}{\partial x_i} \right) - \frac{2}{3} \delta_{ij} \frac{\partial v_k}{\partial x_k} \right], \tag{2.3}$$

where δ_{ij} denotes the Kronecker delta and the Einstein summation convention is applied for all repeated indices.

In OpenFOAM, the incompressible Navier–Stokes equations are solved using solvers such as `simpleFoam` for steady-state flows and `pimpleFoam` or `icoFoam` for transient cases. The pressure–velocity coupling is handled using algorithms such as SIMPLE, PISO, or PIMPLE, depending on whether the flow is steady or unsteady. On this MSc the simpleFoam solver was used for a steady-state flow.

Turbulence Modeling: the k–ω SST

The k–ω Shear Stress Transport (SST) model, developed by Menter [15], is a two-equation turbulence model designed to effectively blend the advantages of the k–ω model near walls and the k–ε model elsewhere. It provides good accuracy for flows with adverse pressure gradients and separation. The equations of turbulent kinetic energy k and the specific dissipation rate ω complete the system of the mean-flow PDEs and are the governing transport equations. The kinetic energy k equation is defined as:

$$R^k = v_j \frac{\partial k}{\partial x_j} - \frac{\partial}{\partial x_j}\left((\nu + \sigma_k \nu_t)\frac{\partial k}{\partial x_j}\right) - A + \beta^* \omega k = 0 \tag{2.4}$$

where β^* is a blended model constant between the k–ε and k–ω (same logic will be applied on rest shared constants):

$$\beta^* = 0.075 F_1 + (1 - F_1)0.09 \tag{2.5}$$

P_k is the production of turbulent kinetic energy

$$P_k = \min\left(\tau_{ij}\frac{\partial u_i}{\partial x_j},\ 10 \cdot \beta^* \rho \omega k\right) \tag{2.6}$$

σ_k is the turbulent Prandtl number for k

$$\sigma_k = 1.85034 F_1 + (1 - F_1)1.0 \tag{2.7}$$

A depends on the turbulence of k and G with

$$A = \min\left[G, c_1 \beta \omega k\right] \tag{2.8}$$

$$G = \nu_t \frac{\partial v_i}{\partial x_j}\left(\frac{\partial v_i}{\partial x_j} + \frac{\partial v_j}{\partial x_i}\right) \tag{2.9}$$

The second equation of the system is governing the specific dissipation rate ω and is written as:

$$R^{\omega} = v_j \frac{\partial \omega}{\partial x_j} - \frac{\partial}{\partial x_j}\left((\nu + \sigma_{\omega}\nu_t)\frac{\partial \omega}{\partial x_j}\right) - \gamma \frac{\partial v_i}{\partial x_j}\left(\frac{\partial v_i}{\partial x_j} + \frac{\partial v_j}{\partial x_i}\right) + \beta\omega^2 - 2\left(1 - F_1\right)\frac{\sigma_{\omega_2}}{\omega}\frac{\partial k}{\partial x_j}\frac{\partial \omega}{\partial x_j} = 0 \tag{2.10}$$

where $\beta = 3/40$, $\sigma_{\omega 2} = 0.856$ are model constants. The σ_{ω} is the blended turbulent Prandtl number for ω and γ is defined as

$$\sigma_{\omega} = 0.5F_1 + (1 - F_1)0.856 \tag{2.11}$$

$$\gamma = 0.5532F_1 + (1 - F_1)0.4403 \tag{2.12}$$

The turbulent viscosity is calculated using:

$$\nu_t = \frac{\rho a_1 k}{\max(a_1\omega, SF_2)} \tag{2.13}$$

where $a_1 = 0.31$ is a model constant, S is the strain rate magnitude and F_2 is a second blending function that will be described below.

$$S = \sqrt{\frac{1}{2}(\frac{\partial v_i}{\partial x_j} + \frac{\partial v_j}{\partial x_i})^2} \tag{2.14}$$

The blending functions F_1 and F_2 govern the transition between the k–ω behavior near the wall and the k–ε behavior in the free stream. Their definitions involve wall distances and model constants the are implemented algorithmically in the CFD software and are calculated for each grid cell.

$$F_1 = \tanh(\arg_1^4) \tag{2.15}$$

where:

$$\arg_1 = \min\left[\min\left[\max\left(\frac{\sqrt{k}}{\beta^*\omega y}, \frac{500\nu}{y^2\omega}\right), \frac{4\rho\sigma_{\omega 2}k}{CD_{k\omega}y^2}\right], 10\right] \tag{2.16}$$

and:

$$CD_{k\omega} = \max\left(2\rho\sigma_{\omega 2}\frac{1}{\omega}\frac{\partial k}{\partial x_j}\frac{\partial \omega}{\partial x_j}, 10^{-10}\right) \tag{2.17}$$

$$F_2 = \tanh(\arg_2^2) \tag{2.18}$$

where:

$$\arg_2 = \min\left(\max\left(\frac{2\sqrt{k}}{\beta^*\omega y},\ \frac{500\nu}{y^2\omega}\right), 100\right) \tag{2.19}$$

where y is the distance from the wall.

Boundary Conditions

The closure of the system of governing equations in CFD is contingent upon the explicit definition of boundary conditions for the entire computational domain. The most prevalent types are the Dirichlet condition, which prescribes a fixed value for a field variable, and the Neumann condition, which specifies a gradient, typically zero. However, some simulations often necessitate the implementation of more complex boundary treatments. Notable among these are wall functions, which provide a computationally efficient model for near-wall turbulence, and hybrid conditions like freestream, which dynamically switch based on local flow direction.

Wall functions in OpenFOAM (and CFD in general) are empirical models used to bridge the near-wall region of turbulent flows, where directly resolving the flow would require an extremely fine mesh (very small y+). They are essential in RANS simulations to reduce computational cost while maintaining reasonable accuracy near solid boundaries, for attached flows. In this MSc thesis, most of the cells of tandem hydrofoils have achieved small enough y+ to allow Low-Re treatment and solve analytically the flow around the walls. The low y+ is the result of various refinement levels and boundary layers.

The free stream is a generic boundary condition that is a hybrid condition which switches between fixed value (Dirichlet) and zero gradient (Neumann) based on the sign of the flow flux.

For the CFD cases solved in this Thesis, the free-stream conditions for the turbulent quantities are given by [16]:

$$\omega_{\text{farfield}} = \frac{\rho k}{\nu}\left(\frac{\nu_t}{\nu}\right)^{-1}$$
$$k_{\text{farfield}} = \frac{3}{2}(vI)^2$$

where:

- $\frac{\nu_t}{\nu} = 10$ is a reasonable value for the viscosity ratio,

- $I = \frac{u'}{\bar{u}} = 5.0\%$ is a hypothetical (rather high) turbulence intensity at farfield.

The above values are assumed for a flow with developed turbulence around the hydrofoils.

Objective Functions and their Differentiation

The objective function of this MSc thesis is the force exerted on the surface of the hydrofoils, projected onto the r_i direction, which is lift for projection on the y-axis & drag for projection on the x-axis. Although these can be both utilized in the objective function which might be in the form of a weighted sum (depending on the case), their calculation remains separated within the adjoint equation solver. The general objective function is written as,

$$F = \int_{S_W} \left(p\delta_i^j - \tau_{ij}\right) r_j n_i dS \tag{2.20}$$

where:

- S_W is the wall surface,
- δ_i^j is the Kronecker delta,
- r_j is a user-defined unit vector defines lift and drag.
- n_i is the outward unit normal vector to the wall.

Considering the generic description of a force F calculated on a surface F_{S_i} is:

$$F = \int_S F_{S_i} n_i dS \tag{2.21}$$

and its differentiation w.r.t. the design variables b_n gives:

$$\frac{\delta F}{\delta b_n} = \int_S \frac{\delta F_{S_i}}{\delta b_n} n_i dS + \int_S F_{S_i} \frac{\delta (n_i dS)}{\delta b_n} \tag{2.22}$$

Assuming that the residuals (as always) of the flow equations are equal to zero, we can add the residuals derivative without altering the equations and apply the chain rule.

$$\frac{\delta R}{\delta b_n} = \frac{\partial R}{\partial b_n} + \frac{\partial R}{\partial x_k} \frac{\delta x_k}{\delta b_n} = 0 \tag{2.23}$$

By applying the chain rule and equation 2.23, we get:

$$\begin{aligned}\frac{\delta F}{\delta b_n} = &\int_S \frac{\partial F_{S_k}}{\partial v_i} n_k \frac{\partial v_i}{\partial b_n} dS + \int_S \frac{\partial F_{S_k}}{\partial p} n_k \frac{\partial p}{\partial b_n} dS \\ &+ \int_S \frac{\partial F_{S_k}}{\partial k} n_k \frac{\partial k}{\partial b_n} dS + \int_S \frac{\partial F_{S_k}}{\partial \omega} n_k \frac{\partial \omega}{\partial b_n} dS \\ &+ \int_S \frac{\partial F_{S_k}}{\partial \tau_{ij}} n_k \frac{\partial \tau_{ij}}{\partial b_n} dS + \int_{S_W} \frac{\partial F_{S_{W,i}}}{\partial x_k} n_i \frac{\delta x_k}{\delta b_n} dS \\ &+ \int_{S_W} F_{S_{W,i}} \frac{\delta (n_i dS)}{\delta b_n}\end{aligned} \tag{2.24}$$

Finally, if we apply the above to the objective function, equation 2.20 and 2.21, it gives:

$$\begin{aligned}\frac{\delta F}{\delta b_n} = &\int_{S_W} \frac{\partial F_{S_{W,k}}}{\partial p} n_k \frac{\partial p}{\partial b_n} dS + \int_{S_W} \frac{\partial F_{S_{W,k}}}{\partial \tau_{ij}} n_k \frac{\partial \tau_{ij}}{\partial b_n} dS \\ &+ \int_{S_W} \frac{\partial F_{S_{W,i}}}{\partial x_k} n_i \frac{\delta x_k}{\delta b_n} dS + \int_{S_W} F_{S_{W,i}} \frac{\delta (n_i dS)}{\delta b_n}\end{aligned} \tag{2.25}$$

where S_W correspondences to the foil surface.

2.3 Continuous Adjoint Method for ShpO

The adjoint method optimization is a powerful technique for computing gradients of objective functions, particularly in the context of optimization in fluid dynamics (CFD), where the governing equations impose a significant computational burden. For ShpO problems in hydrodynamics, where the number of design variables can be very large, adjoint methods provide an efficient way to compute gradients without the prohibitive cost associated with traditional methods such as finite differences.

The optimization problem can be posed as a constrained minimization problem, where the goal is to minimize an objective function F with respect to a set of design variables $\mathbf{b}$, subject to the satisfaction of the governing equations of fluid flow, represented by the residual vector $\mathbf{R}$. The objective function typically depends on both the flow variables $\mathbf{U}$ and the design variables $\mathbf{b}$:

$$F = F(\mathbf{U}, \mathbf{b}). \tag{2.26}$$

For any F, the development of the continuous adjoint method starts by defining the augmented objective function F_{Aug},

$$F_{Aug} = F + \int_{\Omega} \left(u_i R_i^v + q R^p + k_a R^k + \omega_a R^\omega \right) d\Omega \tag{2.27}$$

where u_i, q, k_a and ω_a are the adjoint variables to v_i, p, k and ω respectively and R are the residuals of the field state equations. By employing the Leibniz rule for differentiation under the integral sign,

$$\frac{\delta}{\delta b_n} \int_{\Omega} F(x,t) d\Omega = \int_{\Omega} \frac{\partial F(x,t)}{\partial b_n} d\Omega + \int_S \frac{\delta \overrightarrow{x}}{\delta b_n} F(x,t) \cdot \overrightarrow{n} \, dS \tag{2.28}$$

the derivatives of F_{Aug} w.r.t. b_n become

$$\frac{\delta F_{Aug}}{\delta b_n} = \frac{\delta F}{\delta b_n} + \int_{\Omega} u_i \frac{\partial R_i^v}{\partial b_n} d\Omega + \int_{\Omega} q \frac{\partial R^p}{\partial b_n} d\Omega + \int_{\Omega} k_a \frac{\partial R^k}{\partial b_n} d\Omega + \int_{\Omega} \omega_a \frac{\partial R^\omega}{\partial b_n} d\Omega + \int_S \left(u_i R_i^v + q R^p + k_a R^k + \omega_a R^\omega \right) \frac{\delta x_k}{\delta b_n} n_k dS \tag{2.29}$$

The residuals of the primal equations within the domain are zero,

$$R^\omega = 0 \tag{2.30}$$

$$R^k = 0 \tag{2.31}$$

$$R^p = 0 \tag{2.32}$$

$$R^u = 0 \tag{2.33}$$

The partial derivatives of the residuals of the primal equations (2.1, 2.2, 2.4 & 2.10) w.r.t. to b_n are

$$\frac{\partial R_i^v}{\partial b_n} = \frac{\partial v_j}{\partial b_n} \frac{\partial v_i}{\partial x_j} + v_j \frac{\partial}{\partial x_j} \left(\frac{\partial v_i}{\partial b_n} \right) - \frac{\partial}{\partial x_j} \left(\frac{\partial \tau_{ij}}{\partial b_n} \right) + \frac{\partial}{\partial x_i} \left(\frac{\partial p}{\partial b_n} \right) \tag{2.34}$$

$$\frac{\partial R^p}{\partial b_n} = \frac{\partial}{\partial x_j} \left(\frac{\partial v_j}{\partial b_n} \right) \tag{2.35}$$

$$\frac{\partial R^k}{\partial b_n} = \frac{\partial v_j}{\partial b_n} \frac{\partial k}{\partial x_j} + v_j \frac{\partial}{\partial x_j} \left(\frac{\partial k}{\partial b_n} \right) - \frac{\partial}{\partial x_j} \left(\frac{\partial}{\partial b_n} \left((\nu + \sigma_k \nu_t) \frac{\partial k}{\partial x_j} \right) \right) - \frac{\partial A}{\partial b_n} + \beta^* k \frac{\partial \omega}{\partial b_n} + \beta^* \omega \frac{\partial k}{\partial b_n} \tag{2.36}$$

$$\begin{aligned}\frac{\partial R^{\omega}}{\partial b_n} = &\frac{\partial v_j}{\partial b_n}\frac{\partial \omega}{\partial x_j} + v_j\frac{\partial}{\partial x_j}\left(\frac{\partial \omega}{\partial b_n}\right) - \frac{\partial}{\partial x_j}\left(\frac{\partial}{\partial b_n}\left((\nu+\sigma_\omega\nu_t)\frac{\partial \omega}{\partial x_j}\right)\right) - \\ &\frac{\partial \gamma}{\partial F_1}\frac{\partial F_1}{\partial b_n}\frac{\partial v_i}{\partial x_j}\left(\frac{\partial v_i}{\partial x_j}+\frac{\partial v_j}{\partial x_i}\right) - 2\gamma\left(\frac{\partial v_i}{\partial x_j}+\frac{\partial v_j}{\partial x_i}\right)\frac{\partial}{\partial x_j}\left(\frac{\partial v_i}{\partial b_n}\right) + \\ &\frac{\partial \beta}{\partial F_1}\frac{\partial F_1}{\partial b_n}\omega^2 + 2\beta\omega\frac{\partial \omega}{\partial b_n} + 2\frac{\partial F_1}{\partial b_n}\frac{\sigma_{\omega_2}}{\omega}\frac{\partial k}{\partial x_j}\frac{\partial \omega}{\partial x_j} \\ &+2(1-F_1)\frac{\sigma_{\omega_2}}{\omega^2}\frac{\partial \omega}{\partial b_n}\frac{\partial \omega}{\partial x_j}\frac{\partial k}{\partial x_j} - 2(1-F_1)\frac{\sigma_{\omega_2}}{\omega}\frac{\partial}{\partial x_j}\left(\frac{\partial k}{\partial b_n}\right)\frac{\partial \omega}{\partial x_j} - \\ &2(1-F_1)\frac{\sigma_{\omega_2}}{\omega}\frac{\partial k}{\partial x_j}\frac{\partial}{\partial x_j}\left(\frac{\partial \omega}{\partial b_n}\right) \\ &+B\frac{\partial \omega}{\partial b_n} - B\frac{1}{2\omega\sqrt{\beta^*(\kappa d)^2}}\frac{\partial k}{\partial b_n}\end{aligned} \tag{2.37}$$

The above terms can be further expanded by applying the Green-Gauss theorem to the integrals.

$$\int_\Omega u_i v_j \frac{\partial}{\partial x_j}\left(\frac{\partial v_i}{\partial b_n}\right)d\Omega = \int_S u_i v_j n_j \frac{\partial v_i}{\partial b_n}dS - \int_\Omega \frac{\partial (v_j u_i)}{\partial x_j}\frac{\partial v_i}{\partial b_n}d\Omega \tag{2.38}$$

$$\begin{aligned}&-\int_\Omega u_i \frac{\partial}{\partial x_j}\left(\frac{\partial \tau_{ij}}{\partial b_n}\right)d\Omega = -\int_S u_i n_j \frac{\partial \tau_{ij}}{\partial b_n}dS + \int_S \tau^a_{ij} n_j \frac{\partial v_i}{\partial b_n}dS \\ &-\int_\Omega \frac{\partial \tau^a_{ij}}{\partial x_j}\frac{\partial v_i}{\partial b_n}d\Omega + \int_\Omega \frac{\partial v_i}{\partial x_j}\left(\frac{\partial v_i}{\partial x_j}+\frac{\partial v_j}{\partial x_i}\right)\frac{\partial \nu_t}{\partial b_n}d\Omega\end{aligned} \tag{2.39}$$

$$\int_\Omega u_i \frac{\partial}{\partial x_i}\left(\frac{\partial p}{\partial b_n}\right)d\Omega = \int_S u_i n_j \frac{\partial p}{\partial b_n}dS - \int_\Omega \frac{\partial u_i}{\partial x_i}\frac{\partial p}{\partial b_n}d\Omega \tag{2.40}$$

$$-\int_\Omega q \frac{\partial}{\partial x_j}\left(\frac{\partial v_j}{\partial b_n}\right)d\Omega = -\int_S q n_j \frac{\partial v_j}{\partial b_n}dS + \int_\Omega \frac{\partial q}{\partial x_j}\frac{\partial v_j}{\partial b_n}d\Omega \tag{2.41}$$

$$\int_\Omega k_a v_j \frac{\partial}{\partial x_j}\left(\frac{\partial k}{\partial b_n}\right)d\Omega = \int_S k_a v_j n_j \frac{\partial k}{\partial b_n}dS - \int_\Omega \frac{\partial (v_j k_a)}{\partial x_j}\frac{\partial k}{\partial b_n}d\Omega \tag{2.42}$$

$$\begin{aligned}&-\int_\Omega k_a \frac{\partial}{\partial x_j}\left(\frac{\partial}{\partial b_n}\left((\nu+\sigma_k\nu_t)\frac{\partial k}{\partial x_j}\right)\right)d\Omega = -\int_S k_a n_j \frac{\partial}{\partial b_n}\left((\nu+\sigma_k\nu_t)\frac{\partial k}{\partial x_j}\right)dS \\ &+\int_S (\nu+\sigma_k\nu_t)\frac{\partial k}{\partial x_j}n_j\frac{\partial k}{\partial b_n}dS - \int_\Omega \frac{\partial}{\partial x_j}\left((\nu+\sigma_k\nu_t)\frac{\partial k}{\partial x_j}\right)\frac{\partial k}{\partial b_n}d\Omega\end{aligned}$$

$$+\int_\Omega \frac{\partial k}{\partial x_j}\frac{\partial k}{\partial x_j}\frac{\partial \nu_t}{\partial b_n}d\Omega+\int_\Omega \frac{\partial k}{\partial x_j}\frac{\partial k}{\partial x_j}\frac{\partial \sigma_k}{\partial F_1}\frac{\partial F_1}{\partial b_n}d\Omega \tag{2.43}$$

$$\int_\Omega \omega_a v_j \frac{\partial}{\partial x_j}\left(\frac{\partial \omega}{\partial b_n}\right)d\Omega=\int_S \omega_a v_j n_j \frac{\partial \omega}{\partial b_n}dS-\int_\Omega \frac{\partial(v_j\omega_a)}{\partial x_j}\frac{\partial \omega}{\partial b_n}d\Omega \tag{2.44}$$

$$\begin{aligned}&-\int_\Omega \omega_a \frac{\partial}{\partial x_j}\left(\frac{\partial}{\partial b_n}\left((\nu+\sigma_\omega\nu_t)\frac{\partial \omega}{\partial x_j}\right)\right)d\Omega=-\int_S \omega_a n_j \frac{\partial}{\partial b_n}\left((\nu+\sigma_\omega\nu_t)\frac{\partial \omega}{\partial x_j}\right)dS\\&+\int_S(\nu+\sigma_\omega\nu_t)\frac{\partial \omega}{\partial x_j}n_j\frac{\partial \omega}{\partial b_n}dS-\int_\Omega \frac{\partial}{\partial x_j}\left((\nu+\sigma_\omega\nu_t)\frac{\partial \omega}{\partial x_j}\right)\frac{\partial \omega}{\partial b_n}d\Omega\\&+\int_\Omega \frac{\partial \omega}{\partial x_j}\frac{\partial \omega}{\partial x_j}\frac{\partial \nu_t}{\partial b_n}d\Omega+\int_\Omega \frac{\partial \omega}{\partial x_j}\frac{\partial \omega}{\partial x_j}\frac{\partial F_1}{\partial b_n}d\Omega\end{aligned} \tag{2.45}$$

$$\begin{aligned}&-\int_\Omega \omega_a 2\gamma\left(\frac{\partial v_i}{\partial x_j}+\frac{\partial v_j}{\partial x_i}\right)\frac{\partial}{\partial x_j}\left(\frac{\partial v_i}{\partial b_n}\right)d\Omega=-\int_S 2\gamma\omega_a\left(\frac{\partial v_i}{\partial x_j}+\frac{\partial v_j}{\partial x_i}\right)n_j\frac{\partial v_i}{\partial b_n}dS\\&+\int_\Omega \frac{\partial}{\partial x_j}\left(2\gamma\omega_a\left(\frac{\partial v_i}{\partial x_j}+\frac{\partial v_j}{\partial x_i}\right)\right)\frac{\partial v_i}{\partial b_n}d\Omega\end{aligned} \tag{2.46}$$

$$\begin{aligned}&-\int_\Omega \omega_a 2(1-F_1)\frac{\sigma_{\omega_2}}{\omega}\frac{\partial \omega}{\partial x_j}\frac{\partial}{\partial x_j}\left(\frac{\partial k}{\partial b_n}\right)d\Omega=-\int_S \omega_a 2(1-F_1)\frac{\sigma_{\omega_2}}{\omega}\frac{\partial \omega}{\partial x_j}n_j\frac{\partial k}{\partial b_n}dS\\&+\int_\Omega \frac{\partial}{\partial x_j}\left(\omega_a 2(1-F_1)\frac{\sigma_{\omega_2}}{\omega}\frac{\partial \omega}{\partial x_j}\right)\frac{\partial k}{\partial b_n}d\Omega\end{aligned} \tag{2.47}$$

$$\begin{aligned}&-\int_\Omega \omega_a 2(1-F_1)\frac{\sigma_{\omega_2}}{\omega}\frac{\partial k}{\partial x_j}\frac{\partial}{\partial x_j}\left(\frac{\partial \omega}{\partial b_n}\right)d\Omega=-\int_S \omega_a 2(1-F_1)\frac{\sigma_{\omega_2}}{\omega}\frac{\partial k}{\partial x_j}n_j\frac{\partial \omega}{\partial b_n}dS\\&+\int_\Omega \frac{\partial}{\partial x_j}\left(\omega_a 2(1-F_1)\frac{\sigma_{\omega_2}}{\omega}\frac{\partial k}{\partial x_j}\right)\frac{\partial \omega}{\partial b_n}d\Omega\end{aligned} \tag{2.48}$$

After several simplifications and rearrangements, we conclude to the following equation, where index "a" dictates adjoint variables:

$$\begin{aligned}\frac{\delta F_{Aug}}{\delta b_n}=&\frac{\delta F}{\delta b_n}\\&+\int_\Omega \frac{\partial v_i}{\partial b_n}\Bigg(-\frac{\partial(v_j u_i)}{\partial x_j}+u_j\frac{\partial v_j}{\partial x_i}+\frac{\partial q}{\partial x_i}+k_a\frac{\partial k}{\partial x_i}+\omega_a\frac{\partial \omega}{\partial x_i}-\frac{\partial \tau^a_{ij}}{\partial x_j}\end{aligned}$$

$$
\begin{aligned}
&+ 2\frac{\partial}{\partial x_j}\left(\gamma\omega_a\left(\frac{\partial v_i}{\partial x_j}+\frac{\partial v_j}{\partial x_i}\right)\right)\Bigg)d\Omega - \int_\Omega \frac{\partial p}{\partial b_n}\frac{\partial u_j}{\partial x_j}\,d\Omega \\
&+ \int_\Omega \frac{\partial k}{\partial b_n}\Bigg(-\frac{\partial(v_j k_a)}{\partial x_j} + \beta^* k_a\omega - \frac{\partial}{\partial x_j}\left((\nu+\sigma_k\nu_t)\frac{\partial k_a}{\partial x_j}\right) \\
&\qquad + 2\frac{\partial}{\partial x_j}\left(\omega_a(1-F_1)\frac{\sigma_{\omega 2}}{\omega}\frac{\partial\omega}{\partial x_j}\right) - B\omega_a\frac{1}{2\omega}\sqrt{\frac{\beta^*}{(\kappa d)^2}}\Bigg)d\Omega \\
&+ \int_\Omega \frac{\partial \omega}{\partial b_n}\Bigg(-\frac{\partial(v_j\omega_a)}{\partial x_j} + \beta^* k_a k + 2\beta\omega_a\omega + 2\omega_a(1-F_1)\frac{\sigma_{\omega 2}}{\omega^2}\frac{\partial k}{\partial x_j}\frac{\partial\omega}{\partial x_j} \\
&\qquad + 2\frac{\partial}{\partial x_j}\left(\omega_a(1-F_1)\frac{\sigma_{\omega 2}}{\omega}\frac{\partial k}{\partial x_j}\right) - \frac{\partial}{\partial x_j}\left((\nu+\sigma_\omega\nu_t)\frac{\partial\omega_a}{\partial x_j}\right) + B\omega_a\Bigg)d\Omega \\
&+ \int_\Omega \frac{\partial \nu_t}{\partial b_n}\left(\frac{\partial u_i}{\partial x_j}\left(\frac{\partial v_i}{\partial x_j}+\frac{\partial v_j}{\partial x_i}\right) + \sigma_k\frac{\partial k_a}{\partial x_j}\frac{\partial k}{\partial x_j} + \sigma_\omega\frac{\partial\omega_a}{\partial x_j}\frac{\partial\omega}{\partial x_j}\right)d\Omega \\
&+ \int_\Omega \frac{\partial F_1}{\partial b_n}\Bigg(\nu_t\frac{\partial\sigma_k}{\partial F_1}\frac{\partial k_a}{\partial x_j}\frac{\partial k}{\partial x_j} - \frac{\partial\gamma}{\partial F_1}\omega_a\frac{\partial v_i}{\partial x_j}\left(\frac{\partial v_i}{\partial x_j}+\frac{\partial v_j}{\partial x_i}\right) \\
&\qquad + \frac{\partial\beta}{\partial F_1}\omega_a\omega^2 + \nu_t\frac{\partial\sigma_\omega}{\partial F_1}\frac{\partial\omega_a}{\partial x_j}\frac{\partial\omega}{\partial x_j} + 2\omega_a\frac{\sigma_{\omega 2}}{\omega}\frac{\partial k}{\partial x_j}\frac{\partial\omega}{\partial x_j}\Bigg)d\Omega - \int_\Omega k_a\frac{\partial A}{\partial b_n}\,d\Omega \\
&+ \int_S \frac{\partial v_i}{\partial b_n}\left(u_i v_j n_j - q n_i + (\nu+\nu_t)\left(\frac{\partial u_i}{\partial x_j}+\frac{\partial u_j}{\partial x_i}\right)n_j - 2\gamma\omega_a\left(\frac{\partial v_i}{\partial x_j}+\frac{\partial v_j}{\partial x_i}\right)n_j\right)dS \\
&+ \int_S \frac{\partial p}{\partial b_n}u_i n_i\,dS \\
&+ \int_S \frac{\partial k}{\partial b_n}\left(k_a v_j n_j + (\nu+\sigma_k\nu_t)\frac{\partial k_a}{\partial x_j}n_j - 2\omega_a(1-F_1)\frac{\sigma_{\omega 2}}{\omega}\frac{\partial\omega}{\partial x_j}n_j\right)dS \\
&+ \int_S \frac{\partial \omega}{\partial b_n}\left(\omega_a v_j n_j + (\nu+\sigma_\omega\nu_t)\frac{\partial\omega_a}{\partial x_j}n_j - 2\omega_a(1-F_1)\frac{\sigma_{\omega 2}}{\omega}\frac{\partial k}{\partial x_j}n_j\right)dS \\
&- \int_S u_i n_j\frac{\partial}{\partial b_n}\left((\nu+\nu_t)\left(\frac{\partial v_i}{\partial x_j}+\frac{\partial v_j}{\partial x_i}\right)\right)dS \\
&- \int_S k_a n_j\frac{\partial}{\partial b_n}\left((\nu+\sigma_k\nu_t)\frac{\partial k}{\partial x_j}\right)dS
\end{aligned}
$$

$$
\begin{aligned}
&- \int_S \omega_a n_j \frac{\partial}{\partial b_n} \left((\nu + \sigma_\omega \nu_t) \frac{\partial \omega}{\partial x_j} \right) dS \\
&+ \int_{S_W} \left(u_i R_i^v + q R^p + k_a R^k + \omega_a R^\omega \right) n_k \frac{\delta x_k}{\delta b_n} \, dS
\end{aligned} \tag{2.49}
$$

By further analyzing and differentiating the blending functions $\frac{\partial A}{\partial b_n}$ and $\frac{\partial F_1}{\partial b_n}$ along with their sub terms and transforming them in a differential form, as presented in [18], combined with equation 2.24, we reach the following equation:

$$
\begin{aligned}
\frac{\delta F_{Aug}}{\delta b_n} = &\int_\Omega \left(R_i^u \frac{\partial v_i}{\partial b_n} + R^q \frac{\partial p}{\partial b_n} + R^{k_a} \frac{\partial k}{\partial b_n} + R^{\omega_a} \frac{\partial \omega}{\partial b_n} \right) d\Omega \\
&+ \int_S D_i^u \frac{\partial v_i}{\partial b_n} dS + \int_S D^q \frac{\partial p}{\partial b_n} dS + \int_S D^{k_a} \frac{\partial k}{\partial b_n} dS + \int_S D^{\omega_a} \frac{\partial \omega}{\partial b_n} dS \\
&+ \int_S \left(\frac{\partial F_{S_k}}{\partial \tau_{ij}} n_k - u_i n_j \right) \frac{\partial \tau_{ij}}{\partial b_n} dS - \int_S k_a n_j \frac{\partial}{\partial b_n} \left((\nu + \sigma_k \nu_t) \frac{\partial k}{\partial x_j} \right) dS \\
&- \int_S \omega_a n_j \frac{\partial}{\partial b_n} \left((\nu + \sigma_\omega \nu_t) \frac{\partial \omega}{\partial x_j} \right) dS + \int_{S_W} n_i \frac{\partial F_{S_{W,i}}}{\partial x_k} \frac{\delta x_k}{\delta b_n} dS \\
&+ \int_{S_W} F_{S_i} \frac{\delta (n_i dS)}{\delta b_n} + \int_{S_W} \left(u_i R_i^v + q R^p + k_a R^k + \omega_a R^\omega \right) n_k \frac{\delta x_k}{\delta b_n} dS
\end{aligned} \tag{2.50}
$$

By eliminating all derivatives in the mean-flow and turbulence model variables of equation, 2.50 field integrals w.r.t. the design variables, the field adjoint equations (FEA) are derived:

$$
R^q = -\frac{\partial u_j}{\partial x_j} = 0 \tag{2.51}
$$

$$
\begin{aligned}
R_i^u = &-\frac{\partial (v_j u_i)}{\partial x_j} + u_j \frac{\partial v_j}{\partial x_i} + \frac{\partial q}{\partial x_i} + k_a \frac{\partial k}{\partial x_i} + \omega_a \frac{\partial \omega}{\partial x_i} - \frac{\partial \tau_{ij}^a}{\partial x_j} \\
&+ 2 \frac{\partial}{\partial x_j} \left(\left(P_1^A k_a \nu_t + \gamma \omega_a + P_2^{\nu_t} \frac{C_{\Omega,\nu_t} a_1 k}{2 \mathcal{S}_t^3 F_2} \right) \left(\frac{\partial v_i}{\partial x_j} + \frac{\partial v_j}{\partial x_i} \right) \right) = 0
\end{aligned} \tag{2.52}
$$

$$
R^{k_a} = -v_j \frac{\partial k_a}{\partial x_j} - \frac{\partial}{\partial x_j} \left((\nu + \sigma_k \nu_t) \frac{\partial k_a}{\partial x_j} \right) + 2 \frac{\partial}{\partial x_j} \left(\omega_a (1 - F_1) \frac{\sigma_{\omega_2}}{\omega} \frac{\partial \omega}{\partial x_j} \right) +
$$

$$(1-P_2^A c_1)\beta^* k_a \omega + \frac{\partial \nu_t}{\partial k} C_{\Omega,\nu_t} + \frac{\partial F_1}{\partial k} C_{\Omega,F_1} + \frac{\partial}{\partial x_i}\left(C_{\Omega,F_1} \frac{\partial F_1}{\partial \left(\frac{\partial k}{\partial x_i}\right)} \right) - B \frac{\omega_a}{2\omega\sqrt{\beta^*(\kappa d)^2}} = 0 \tag{2.53}$$

$$\begin{aligned} R^{\omega_a} = -v_j \frac{\partial \omega_a}{\partial x_j} - \frac{\partial}{\partial x_j}\left((\nu + \sigma_\omega \nu_t)\frac{\partial \omega_a}{\partial x_j}\right) + 2\frac{\partial}{\partial x_j}\left(\omega_a (1-F_1)\frac{\sigma_{\omega_2}}{\omega}\frac{\partial k}{\partial x_j}\right) + \\ 2\omega_a (1-F_1)\frac{\sigma_{\omega_2}}{\omega^2}\frac{\partial k}{\partial x_j}\frac{\partial \omega}{\partial x_j} + 2\beta\omega_a\omega + (1-P_2^A c_1)\beta^* k_a k + \frac{\partial \nu_t}{\partial \omega} C_{\Omega,\nu_t} \\ + \frac{\partial F_1}{\partial \omega} C_{\Omega,F_1} + \frac{\partial}{\partial x_i}\left(C_{\Omega,F_1} \frac{\partial F_1}{\partial \left(\frac{\partial \omega}{\partial x_i}\right)} \right) + B\omega_a = 0 \end{aligned} \tag{2.54}$$

where the coefficients C_{Ω,ν_t} and C_{Ω,F_1} are defined as:

$$C_{\Omega,\nu_t} = \frac{\partial u_i}{\partial x_j}\left(\frac{\partial v_i}{\partial x_j} + \frac{\partial v_j}{\partial x_i}\right) + \sigma_k \frac{\partial k}{\partial x_j}\frac{\partial k_a}{\partial x_j} + \sigma_\omega \frac{\partial \omega}{\partial x_j}\frac{\partial \omega_a}{\partial x_j} - P_1^A k_a \frac{\partial v_i}{\partial x_j}\left(\frac{\partial v_i}{\partial x_j} + \frac{\partial v_j}{\partial x_i}\right) \tag{2.55}$$

$$C_{\Omega,F_1} = \nu_t \sigma_k^\Delta \frac{\partial k_a}{\partial x_j}\frac{\partial k}{\partial x_j} - \gamma^\Delta \omega_a \frac{\partial v_i}{\partial x_j}\left(\frac{\partial v_i}{\partial x_j} + \frac{\partial v_j}{\partial x_i}\right) + \beta^\Delta \omega_a \omega^2 + \nu_t \sigma_\omega^\Delta \frac{\partial \omega_a}{\partial x_j}\frac{\partial \omega}{\partial x_j} + 2\omega_a \frac{\sigma_{\omega_2}}{\omega}\frac{\partial k}{\partial x_j}\frac{\partial \omega}{\partial x_j} \tag{2.56}$$

where $\sigma_k^\Delta = \sigma_k^1 - \sigma_k^2$ (similarly β^Δ & σ_ω^Δ)and the coefficients P_1^A, P_2^A and $P_2^{\nu_t}$ are defined as:

$$P_1^A = \begin{cases} 1 & \text{if } G < c_1\beta^*\omega k, \\ 0 & \text{else,} \end{cases} \qquad P_2^A = 1 - P_1^A \tag{2.57}$$

$$P_1^{\nu_t} = \begin{cases} 1 & \text{if } a_1\omega > \mathcal{S}_t F_2, \\ 0 & \text{else,} \end{cases} \qquad P_2^{\nu_t} = 1 - P_1^{\nu_t} \tag{2.58}$$

where G is defined in equation 2.9.

$R^q = 0$ is the adjoint continuity equation and $R_i^u = 0$ the adjoint momentum equations, together consisting the adjoint mean-flow equations. The $R^{ka} = 0$ and $R^{\omega a} = 0$ are the adjoint turbulence model equations. The adjoint continuity equation enforces a divergence free adjoint velocity vector, while the adjoint momentum equations include an adjoint convection term and an adjoint transpose convection (ATC) term, both originating from the

differentiation of the convection term, an adjoint stresses term and an adjoint pressure gradient. All these terms are the adjoint counterparts to the primal momentum terms.

The D coefficients in equation 2.50 are defined as follows and they contribute to the adjoint boundary conditions:

$$D_i^u = u_i v_j n_j - q n_i + \tau_{ij}^a n_j - 2\left(\gamma\omega_a + P_1^A k_a \nu_t + P_2^{\nu_t}\frac{C_{\Omega,\nu_t} a_1 k}{2\mathcal{S}_t^3 F_2}\right)\left(\frac{\partial v_i}{\partial x_j} + \frac{\partial v_j}{\partial x_i}\right) n_j + \frac{\partial F_{S_k}}{\partial v_i} n_k \tag{2.59}$$

$$D^q = u_i n_i + \frac{\partial F_{S_k}}{\partial p} n_k \tag{2.60}$$

$$D^{k_a} = k_a v_j n_j + (\nu + \sigma_k \nu_t)\frac{\partial k_a}{\partial x_j} n_j - 2\omega_a(1 - F_1)\frac{\sigma_{\omega_2}}{\omega}\frac{\partial \omega}{\partial x_j} n_j + \frac{\partial F_{S_k}}{\partial k} n_k \tag{2.61}$$

$$D^{\omega_a} = \omega_a v_j n_j + (\nu + \sigma_\omega \nu_t)\frac{\partial \omega_a}{\partial x_j} n_j - 2\omega_a(1 - F_1)\frac{\sigma_{\omega_2}}{\omega}\frac{\partial k}{\partial x_j} n_j + \frac{\partial F_{S_k}}{\partial \omega} n_k \tag{2.62}$$

Finally, the sensitivity derivatives are given by:

$$\begin{aligned}
\frac{\delta F}{\delta b_n} = &- \int_{S_W} \left(\tau_{ij}^a n_j - q n_i - P_2^{\nu_t}\frac{C_{\Omega,\nu_t} a_1 k}{S_t^3 F_2}\left(\frac{\partial v_i}{\partial x_j} + \frac{\partial v_j}{\partial x_i}\right) n_j + \frac{\partial F_{S_W,k}}{\partial v_i} n_k\right)\frac{\partial v_i}{\partial x_k}\frac{\delta x_k}{\delta b_n} dS \\
&+ \int_{S_W} k_a(\nu + \sigma_k \nu_t)\frac{\partial}{\partial x_k}\left(\frac{\partial k}{\partial x_j} n_j\right)\frac{\delta x_k}{\delta b_n} dS \\
&+ \int_{S_W} \left(k_a(\nu + \sigma_k \nu_t) + \frac{\partial F_{S_W,k}}{\partial k} n_k\right)\frac{\partial k}{\partial x_j}\frac{\delta n_j}{\delta b_n} dS \\
&+ \int_{S_W} \omega_a(\nu + \sigma_\omega \nu_t)\frac{\partial}{\partial x_k}\left(\frac{\partial \omega}{\partial x_j} n_j\right)\frac{\delta x_k}{\delta b_n} dS \\
&+ \int_{S_W} \left(\omega_a(\nu + \sigma_\omega \nu_t) + \frac{\partial F_{S_W,k}}{\partial \omega} n_k\right)\frac{\partial \omega}{\partial x_j}\frac{\delta n_j}{\delta b_n} dS \\
&+ \int_{S_W} n_i \frac{\partial F_{S_W,i}}{\partial x_k} n_k \frac{\delta x_l}{\delta b_n} dS + \int_{S_W} F_{S_W,i}\frac{\delta(n_i dS)}{\delta b_n} \\
&+ \int_{S_W} \left(u_i R_i^v + q R^p + k_a R^k + \omega_a R^\omega\right) n_k \frac{\delta x_k}{\delta b_n} dS
\end{aligned}$$

$$
\begin{aligned}
&- \int_{S_W} \left[\left(-u_k n_k + \frac{\partial F_{S_W,k}}{\partial \tau_{lz}} n_k n_l n_z \right) \left(\tau_{ij} \frac{\delta (n_i n_j)}{\delta b_n} + \frac{\partial \tau_{ij}}{\partial x_z} n_z \frac{\delta x_k}{\delta b_n} n_k n_i n_j \right) \right] dS \\
&- \int_{S_W} \left[\frac{\partial F_{S_W,k}}{\partial \tau_{lz}} n_k t_l^I t_z^I \left(\tau_{ij} \frac{\delta (t_i^I t_j^I)}{\delta b_n} + \frac{\partial \tau_{ij}}{\partial x_z} n_z \frac{\delta x_k}{\delta b_n} n_k t_i^I t_j^I \right) \right] dS \\
&- \int_{S_W} \left[\left(\frac{\partial F_{S_W,k}}{\partial \tau_{lz}} n_k (t_l^{II} t_z^I + t_l^I t_z^{II}) \right) \left(\tau_{ij} \frac{\delta (t_i^{II} t_j^I)}{\delta b_n} + \frac{\partial \tau_{ij}}{\partial x_z} n_z \frac{\delta x_k}{\delta b_n} n_k t_i^{II} t_j^I \right) \right] dS \\
&- \int_{S_W} \left[\frac{\partial F_{S_W,k}}{\partial \tau_{lz}} n_k t_l^{II} t_z^{II} \left(\tau_{ij} \frac{\delta (t_i^{II} t_j^{II})}{\delta b_n} + \frac{\partial \tau_{ij}}{\partial x_z} n_z \frac{\delta x_k}{\delta b_n} n_k t_i^{II} t_j^{II} \right) \right] dS
\end{aligned}
\tag{2.63}
$$

5. Adjoint Boundary Conditions

The adjoint boundary conditions can be extracted from the surface integrals and are dependent on the chosen objective function, which in this MSc thesis is the force exerted on the foils. More detailed the:

Wall conditions:

To eliminate the integrals containing $\frac{\partial k}{\partial b_n}$ and $\frac{\partial \omega}{\partial b_n}$, the following boundary conditions are being imposed on k_a and ω_a along the wall

$$(\nu + \sigma_k \nu_t) \frac{\partial k_a}{\partial x_j} n_j = -\frac{\partial F_{S_{W,i}}}{\partial k} n_i \tag{2.64}$$

$$(\nu + \sigma_\omega \nu_t) \frac{\partial \omega_a}{\partial x_j} n_j = -\frac{\partial F_{S_{W,i}}}{\partial \omega} n_i \tag{2.65}$$

yielding Neumann type conditions at the wall.

Due to the no-slip condition, $v_i = 0$, the derivatives of the velocity components are $\frac{\delta v_i}{\delta b_n} = 0$ which give

$$\frac{\partial v_i}{\partial b_n} = -\frac{\partial v_i}{\partial x_k} \frac{\delta x_k}{\delta b_n} \tag{2.66}$$

$$\frac{\partial v_i}{\partial b_n} = -\frac{\partial v_i}{\partial x_k} \frac{\delta x_k}{\delta b_n} \tag{2.78}$$

Finally, to eliminate the rest of unwanted integrals, the below boundary conditions apply along the walls:

$$u_j n_j = -\frac{\partial F_{S_{W,i}}}{\partial p} n_i \tag{2.67}$$

$$\tag{2.68}$$

$$u_i t_i^I = \frac{\partial F_{S_{W,k}}}{\partial \tau_{ij}} n_k t_i^I n_j + \frac{\partial F_{S_{W,k}}}{\partial \tau_{ij}} n_k t_j^I n_i \tag{2.69}$$

$$u_i t_i^{II} = \frac{\partial F_{S_{W,k}}}{\partial \tau_{ij}} n_k t_i^{II} n_j + \frac{\partial F_{S_{W,k}}}{\partial \tau_{ij}} n_k t_j^{II} n_i \tag{2.70}$$

where the t_i^I and t_i^{II} are the components of the tangent to the surface vectors [19].

Inlet boundary conditions:

Along the inlet boundary, due to the primal Dirichlet conditions $\frac{\delta v_i}{\delta b_n} = \frac{\delta k}{\delta b_n} = \frac{\delta \omega}{\delta b_n} = 0$ and equation 2.71, the boundary integrals which are unwanted are eliminated:

$$u_j n_j = -\frac{\partial F_{S_{I,i}}}{\partial p} n_i \tag{2.71}$$

$$u_i t_i^I = \frac{\partial F_{S_{I,k}}}{\partial \tau_{ij}} n_k t_i^I n_j + \frac{\partial F_{S_{I,k}}}{\partial \tau_{ij}} n_k t_j^I n_i \tag{2.72}$$

$$u_i t_i^{II} = \frac{\partial F_{S_{I,k}}}{\partial \tau_{ij}} n_k t_i^{II} n_j + \frac{\partial F_{S_{I,k}}}{\partial \tau_{ij}} n_k t_j^{II} n_i \tag{2.73}$$

Also, for the same purpose we impose:

$$k_a = 0 \tag{2.74}$$

$$\omega_a = 0 \tag{2.75}$$

Outlet boundary conditions:

Due to the zero Neumann conditions on v_i, k_i and ω, the fixed pressure boundary condition, and equations

$$D_i^u = 0 \tag{2.76}$$

$$D^{k_a} = 0 \tag{2.77}$$

$$D^{\omega_a} = 0 \tag{2.78}$$

the remaining integrals along the outlet boundary S_o are eliminated, which lead to a Robin type boundary condition for k_a and ω_a and has to be decomposed into the normal and tangent directions as

$$q = u_i n_i v_j n_j + \tau_{ij}^a n_j n_i + \frac{\partial F_{S_{O,k}}}{\partial v_i} n_k n_i$$

$$- 2 \left(P_1^A \nu_t k_a + \gamma \omega_a + P_2^{\nu_t} \frac{C_{\Omega,\nu_t} a_1 k}{2\mathcal{S}^3 F_2} \right) \left(\frac{\partial v_i}{\partial x_j} + \frac{\partial v_j}{\partial x_i} \right) n_j n_i \tag{2.79}$$

$$u_i t_i^I v_j n_j + \tau_{ij}^a n_j t_i^I - q n_i t_i^I + \frac{\partial F_{S_{O,k}}}{\partial v_i} n_k t_i^I$$
$$- 2 \left(P_1^A \nu_t k_a + \gamma \omega_a + P_2^{\nu_t} \frac{C_{\Omega,\nu_t} a_1 k}{2\mathcal{S}^3 F_2} \right) \left(\frac{\partial v_i}{\partial x_j} + \frac{\partial v_j}{\partial x_i} \right) n_j t_i^I = 0 \tag{2.80}$$

$$u_i t_i^{II} v_j n_j + \tau_{ij}^a n_j t_i^{II} - q n_i t_i^{II} + \frac{\partial F_{S_{O,k}}}{\partial v_i} n_k t_i^{II} \tag{2.81}$$
$$- 2 \left(P_1^A \nu_t k_a + \gamma \omega_a + P_2^{\nu_t} \frac{C_{\Omega,\nu_t} a_1 k}{2\mathcal{S}^3 F_2} \right) \left(\frac{\partial v_i}{\partial x_j} + \frac{\partial v_j}{\partial x_i} \right) n_j t_i^{II} = 0$$

2.4 Function minimization by steepest descent

Solving the primal and adjoint equations allows the computation of the sensitivity derivatives ($\frac{\delta J}{\delta b_i}$) of said function and the modification of the design variables δb_i (e.g. control points) to achieve the optimization targets. Following the computation of sensitivity derivatives, the update vector is computed through the steepest descent method.

$$b_i{}^{new} = b_i{}^{old} - \eta \frac{\delta J}{\delta b_i} \tag{2.82}$$

where the search direction is defined directly by the negative sensitivity derivative ($\frac{\delta J}{\delta b_i}$). The value of η is defined by the user on each case separately and defines the impact the update has at the design variables, in each optimization cycle. Thus, it determines how fast or slow the optimization proceeds.

When performing ShpO, the design variables control the hydrodynamic shape. An practical approach is to enclose the object under optimization within a closed region, made by a structured "grid" of points. These control points of which the coordinates will act as the design variables for the optimization problem, will be connected with the actual grid through a parameterization mapping and will act as B-Splines. Given the control points position, the knot vectors and the basis functions degrees, which needs to be computed only once, the parametric coordinates of a point with Cartesian coordinates within the grid can be found.

Having said the above, following the computation of the sensitivities on the control points and by adjusting their position, the new Cartesian coordinates of each (internal or boundary) mesh point residing within the control

grid can be computed, making volumetric B-splines a powerful surface parameterization and mesh displacement tool [20].

The adjoint ShpO workflow, considering the case is already set up, is as follows:

1. solve the primal mean flow and the flow equations
2. compute the objective function J
3. solve the adjoint mean flow and adjoint k-ω SST turbulence flow equations.
4. compute sensitivity derivatives
5. update the design variables b
6. update the geometry to be designed and the volumetric B-splines
7. repeat.

Chapter 3

CFD Analysis

The Reynolds number of the subject studies is occurring through the real-world marine and aerodynamic applications involving hydrofoils and is set to 10^6. This value is sufficiently high to avoid transitional or laminar behavior and guarantee, that the flow remains fully turbulent across the domain. The high Reynolds number also justifies the use of turbulence models and allows the investigation of effect that has the wake of fore hydrofoil to the aft.

The common position angle of the hydrofoils was set to 9° a value selected to balance two critical objectives and the infinite flow angle to 0°Ḟirst, it is large enough to provoke significant interaction between the tandem hydrofoils, thereby allowing the study of wake interference and induced turbulence effects. Second, it remains below the stall angle, thus avoiding flow separation that could complicate the analysis and introduce numerical instability. This choice ensures that the hydrofoils operate in a stable yet sensitive region of their performance curve, making it ideal for comparative analysis.

By examining both isolated and tandem arrangements under identical flow conditions, the influence of hydrofoil interaction on lift, drag, and turbulence characteristics can be effectively evaluated.

3.1 Single Hydrofoil Solution

The first studied case will be for an NACA4412 at 0° infinite flow and 9° position angle, setting the foundations of the following cases by means of grid size, refinement level, boundary layer and of the flow initial conditions. Based on this simple case, which can be compared with others from the literature, we setup the case prior to the tandem scenarios.

Mesh Independence Study

The mesh was generated through snappyHexMesh and blockMesh libraries of openFoam. The primary function of blockMesh in this study was to generate the background computational mesh, which was structured with varying cell densities along the i and j directions (blockMesh creates structured meshes). These variations allow for control over the global mesh resolution, with denser configurations representing a higher total number of computational cells. Following the generation of the background mesh, the snappyHexMesh (sHM) utility was employed to insert the surfaces of foils by snapping on them and perform local mesh refinement in the vicinity of each hydrofoil geometry (snappyHexMesh creates unstructured meshes). These refined zones, referred to as cell refinement regions, were introduced to better capture the complex flow phenomena around the hydrofoil locally and avoid denser mesh globally. Each refinement level applied using sHM effectively doubled the number of cells in the specified region, thereby enhancing local resolution. The last feature utilized by sHM was the boundary layer (BL) generation our the snapped geometry, which allow a smooth transition from wall region to the developed flow around the hydrofoils. The overall control of mesh resolution was governed by the initial base mesh density generated by blockMesh, with refinement parameters and configurations detailed in the table below.

Mesh	i	j	Cells	Cd	Cl	% Change Cd	% Change Cl
Coarse	126	70	52492	0.008323	0.466637	1.91%	0.17%
Medium	180	100	97915	0.008314	0.469829	0.49%	0.67%
Fine	234	130	152345	0.008422	0.466491	-	-

Table 3.1: Results of mesh independence study on 0° common common position angle.

Mesh	i	j	Cells	Cd	Cl	% Change Cd	% Change Cl
Coarse	126	70	56832	0.0376	1.365	20.91%	1.03%
Medium	180	100	101716	0.0332	1.363	8.49%	0.88%
Fine	234	130	161955	0.0306	1.351	-	-

Table 3.2: The results of mesh independence study on 9° common position angle.

Figure 3.1, 3.2 and 3.3 present the generated grid with 101716 cells.

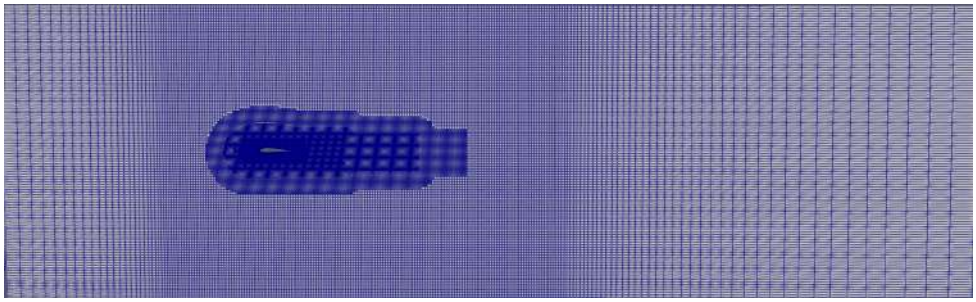

Figure 3.1: The generated grid for one hydrofoil at 0° common position angle.

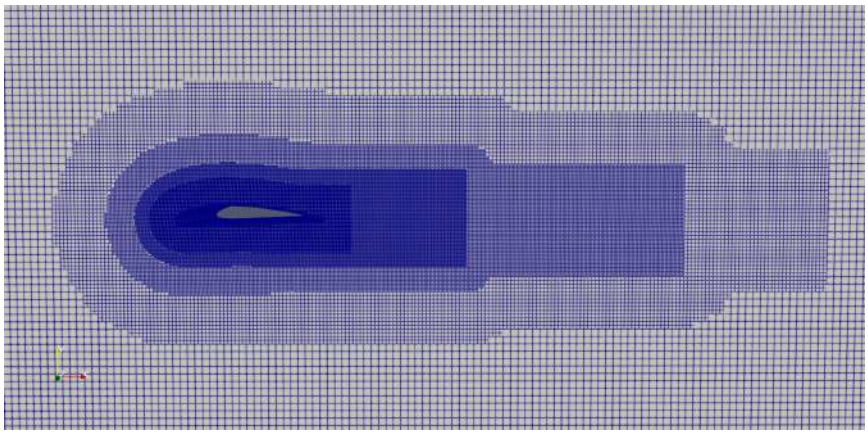

Figure 3.2: Close-up view at the refinement levels and areas around the foil.

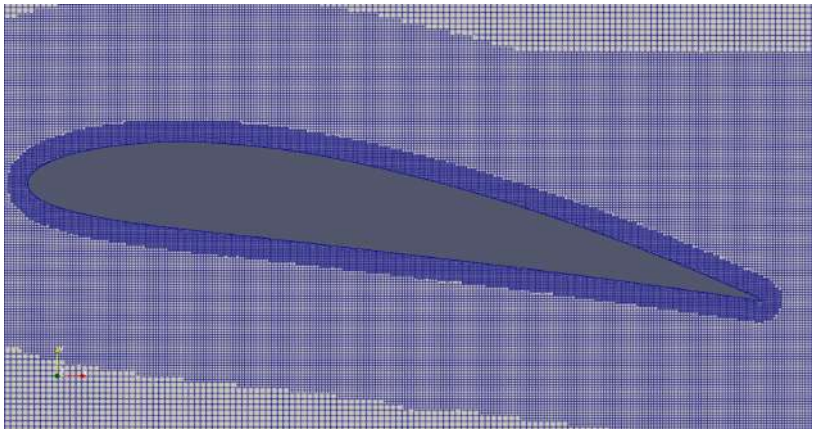

Figure 3.3: The generated grid around the foil and the boundary layer.

The purpose of this comparison is to prove that the methodology and tools utilized for the CFD analysis that will follow, are accurate based on

the literature and common practices. For sake of completeness, the results computed through openFoam and X-foil [21], and uses Boundary Element Method (BEM) to compute the pressure distribution, are compared for the same parameters at table 3.3.

Method	C_l
OpenFOAM	1.363
XFOIL	1.3749

Table 3.3: Results of OpenFOAM and XFOIL.

In the next chapters, the medium grid (101716 cells) will be utilized for single hydrofoil ShpO. By this mesh independence study the optimal parameters for the set up of the tandem grids, the refinement levels required and the number of boundary layers around each foil have been derived.

3.2 Two hydrofoils in tandem

This section focuses on the investigation of two hydrofoils arranged in a tandem configuration. The introduction of a second hydrofoil within the grid, revealed several challenges that needed to be addressed before obtaining reliable computational results. Despite these challenges, the effort proved to be worthwhile, as the final results unlocked valuable insights. The total number of grid cells increased significantly due to the duplication of all refinement levels for the second hydrofoil, as well as the expansion of the background domain to capture the extended wake of the first hydrofoil.

A parametric study was conducted to determine the spacing between the two hydrofoils for the studied scenarios. Based on this analysis, an edge-to-edge distance L of 4 chord-lengths (4C) was selected for (and fixed during) the optimization cycles presented in Chapter 4. This distance was chosen because, at shorter spacings, the fore hydrofoil exhibited negative drag coefficients (C_d), which is practically unphysical for real life marine application. The spacing study was carried out in increments of 0.5C.

The drag and lift coefficients for each tested spacing are presented in figures 3.4 and 3.5. As expected, increasing the distance between the hydrofoils reduces their hydrodynamic interaction. In practical applications, additional factors would influence the selection of this spacing; however, in the context of this parametric study, the primary concern is understanding the fundamental flow physics.

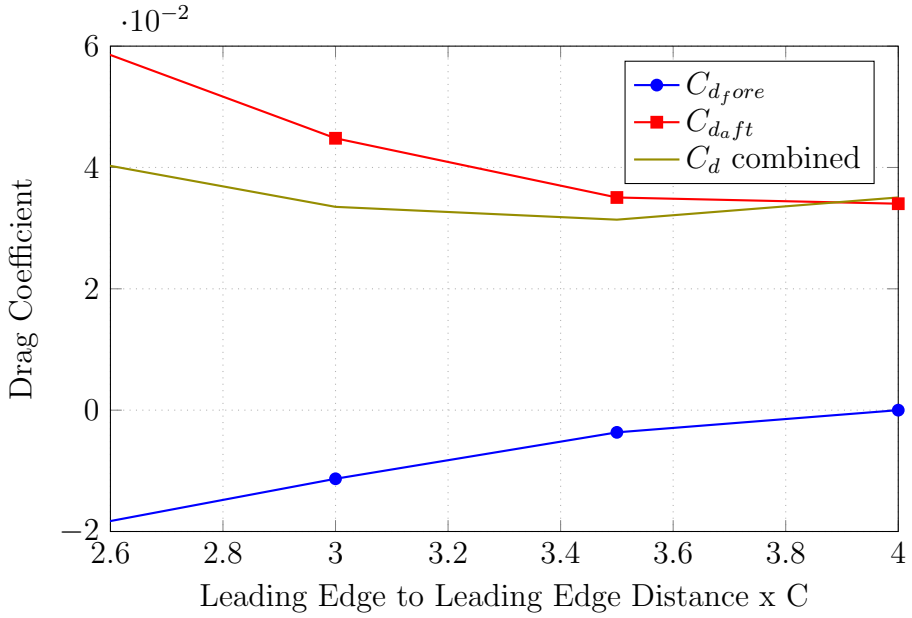

Figure 3.4: Dependence of the drag coeddicient (of the fore- and aft- foils, as well as cumulative) on L, for two hydrofoils at 9° common position angle.

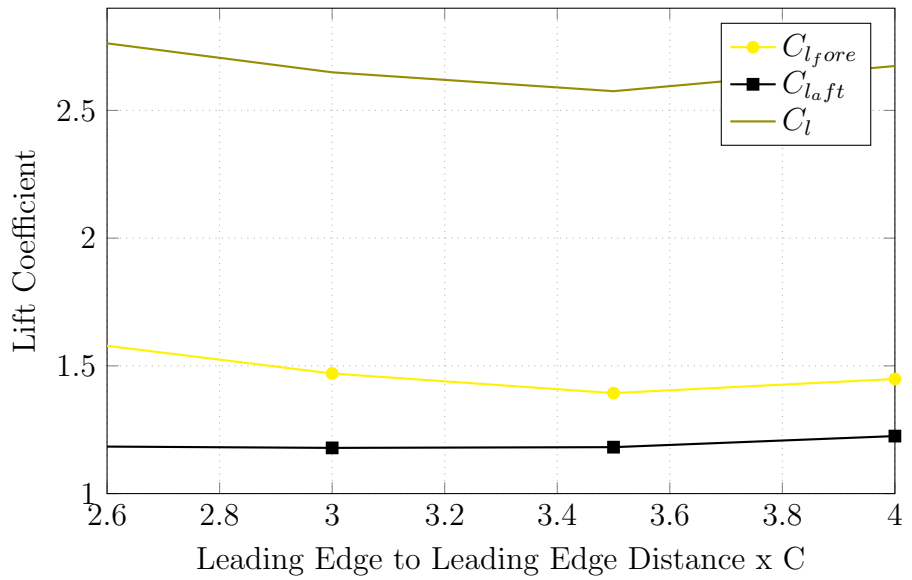

Figure 3.5: Dependence of the lift coefficient (of the fore - and aft - foils, as well as cumulative) on L, for two hydrofoils at 9° common position angle.

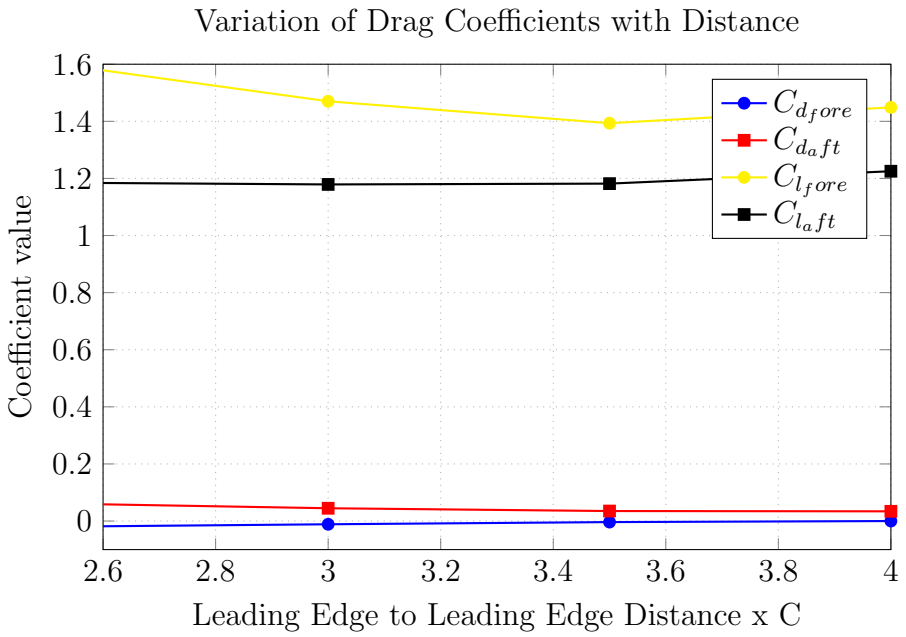

Figure 3.6: Dependence of the force coefficient (of the fore- and aft- foils, as well as cumulative) on L, for two hydrofoils at 9° common position angle.

Grid Independence

The grid generated for the tandem mode hydrofoils followed the same pattern that was used for the single foil and it included a limited quantity of boundary layers around the foils that assisted in solving smoothly the adjoint equations. A background grid with dense cells was utilized around the areas of interest and several refinement levels were implemented around the hydrofoils or their wake. This avoids a uniformly defined grid and reduces the total amount of cells by keeping also the accuracy high.

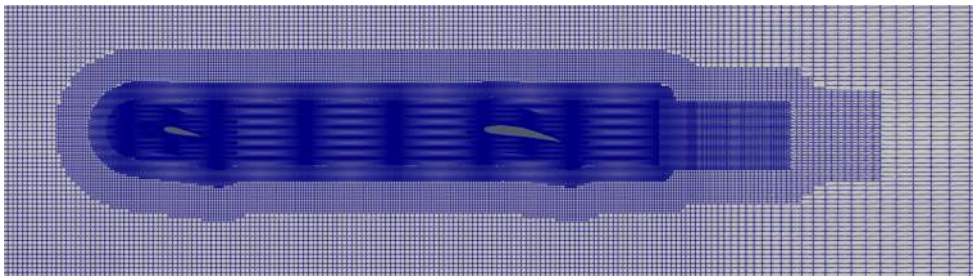

Figure 3.7: The generated grid for edge-to-edge distance at 4 chords

The grid independence was made at grids with a fixed cell dimension

aspect ratio of 1.8 and the change below 2 % was achieved at 271613 cells. The coefficient utilized as a criterion for the independency study was the lift, that remain the main objective studied in this thesis.

Grid	i Cells	j Cells	Total Cells
Coarse	162	90	232526
Mid Fine	180	100	271613
Fine	198	111	312231

Table 3.4: Grid resolution details for the tandem hydrofoil study, i and j are referring to the initial structured grid generated though blockMesh.

The fine grid achieved a change of 0.74% at $C_{l_{fore}}$ and 0.55% at $C_{l_{aft}}$ that are both well below the 1% limit and considered acceptable. Having completed the above grid independence study (tables 3.5 & 3.6), we have reached a final grid that can be utilized for the optimization scenarios that will follow in the next chapter. This was a step that needed to ensure accurate computation of forces and align with common practices of the industry.

Figure 3.8: Velocity distribution around both hydrofoils at Re 10^6, for two hydrofoils at 9° common position angle.

The pressure distribution over a hydrofoil (Figure 3.09 & 3.10) is a direct manifestation of the local flow velocity, as described by Bernoulli's principle. As expected, an initial observation is that the qualitative pattern of the pressure distribution—characterized by the suction side and high pressure side —is nearly identical for both foils. This is a direct consequence of their identical geometric shape and angle of attack.

Grid	Cd_1	Cl_1	$\%\Delta Cd_1$	$\%\Delta Cl_1$
Coarse	0.0164245	1.393891	-	-
Mid Fine	0.0160292	1.3874226	-2.47%	-0.47%
Fine	0.0144765	1.397836	-10.73%	0.74%

Table 3.5: Lift and drag coefficients and relative changes with increasing grid resolution, for the fore foil at 9° common position angle.

Grid	Cd_2	Cl_2	$\%\Delta Cd_2$	$\%\Delta Cl_2$
Coarse	0.0424703	1.188014	-	-
Mid Fine	0.0414361	1.180148	2.50%	-0.67%
Fine	0.0410385	1.186638	-0.97%	0.55%

Table 3.6: Lift and drag coefficients and relative changes with increasing grid resolution, for the aft foil at 9° common position angle.

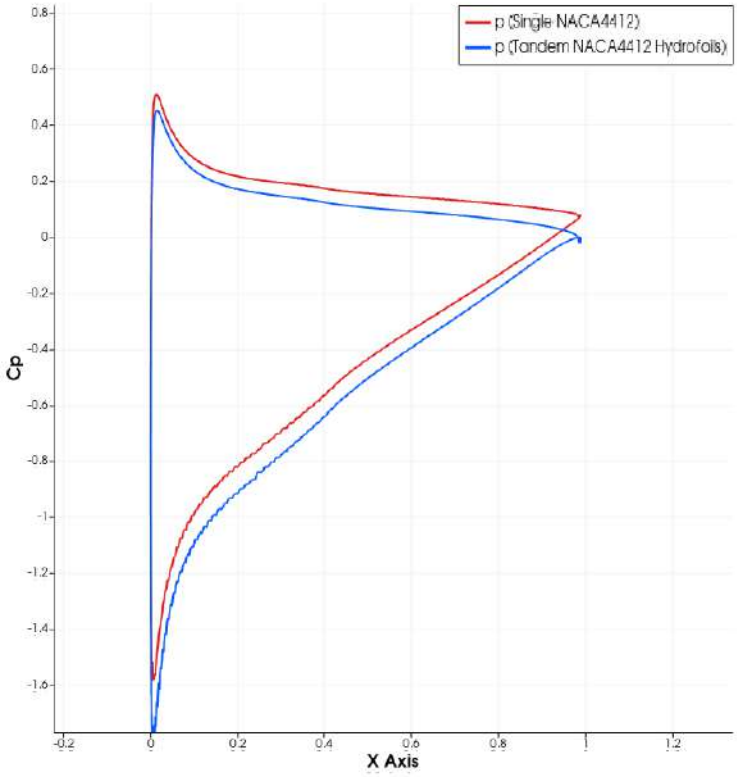

Figure 3.9: Pressure distribution around the fore hydrofoil with single foil and tandem foils, for two hydrofoils at 9° common position angle.

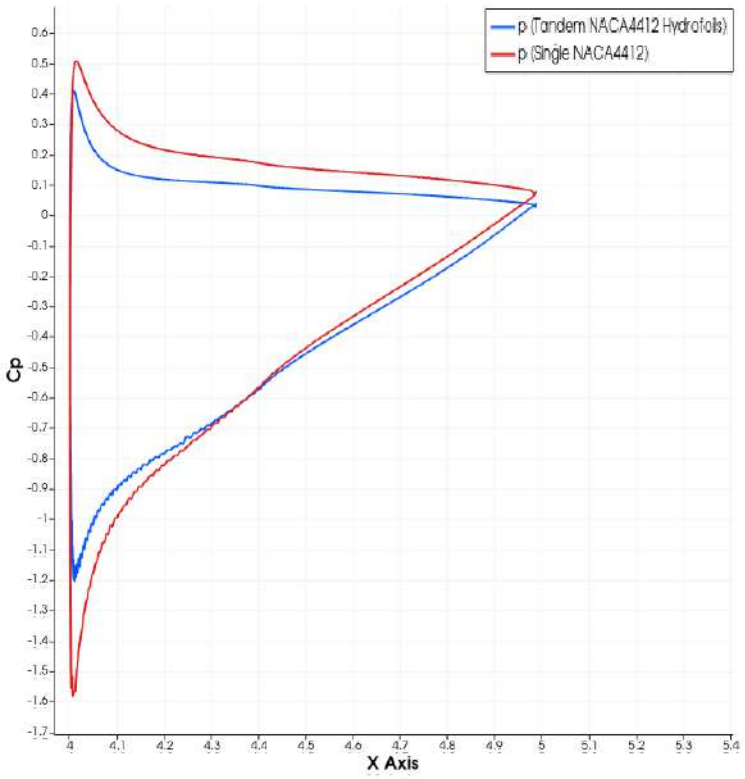

Figure 3.10: Pressure distribution around the aft hydrofoil, for two hydrofoils at 9° common position angle.

However, this geometric similarity belies a significant quantitative difference in the flow conditions each foil experiences, which is the effective inflow velocity. The fore foil encounters the undisturbed freestream velocity (U_∞). In contrast, the aft foil operates within the wake of the fore foil, a region of velocity deficit and increased turbulence.

The quantitative comparison of the C_p values (both minimum and maximum) between the tandem foils and an isolated, single foil of the same geometry reveals this interaction clearly:

- **The fore foil exhibits increased pressure difference between upper/lower side:** The presence of the aft foil influences the pressure field of the fore foil by increasing the local flow velocity over the fore foil, which leads to a lower minimum pressure on its suction side and a higher maximum pressure on its pressure side, compared to the isolated case. This indicates the fore foil is generating a higher lift coefficient (C_l) than it would in isolation.

- **The aft foil exhibits decreased pressure difference between upper/lower side:** The aft foil experiences a reduced effective inflow velocity due to the wake of the fore foil. While the upwash from the fore foil may increase its effective angle of attack, the dominant effect in this optimized configuration is often the velocity deficit. This results in a less intense pressure differential across the aft foil, with consequently reduced C_l compared to the isolated foil.

This redistribution of load—where the fore foil is more heavily loaded and the aft foil is less loaded—is a classic and well-documented phenomenon in tandem wing aerodynamics [22, 23]. The present results provide clear quantitative evidence of this effect within the hydrodynamic context too. The fore foil is leveraged to do more lifting work, while the aft foil benefits from the accelerated and turned flow, albeit at a reduced individual efficiency, leading to a superior combined performance.

Chapter 4

Adjoint Optimization

In this chapter, a series of optimization cases are presented based on the *Mid Fine Mesh* presented in Chapter 3, which features a tandem hydrofoil configuration as described. The individual studies differ in terms of their optimization objectives and the specific components of the tandem system to which the optimization is applied.

While the primary objective across all cases is the maximization of the hydrofoil's lift (individually or as a group)—recognized as a critical performance metric—several cases also incorporate drag minimization. Including drag as a secondary objective helps avoiding extreme or non-physical geometrical modifications, leading to more realistic and efficient designs, while it can also highlight the impact ShpO has on the applied forces.

The following optimization cases are analyzed:

- **Case 1:** Lift maximization of the aft foil.
- **Case 2:** Lift maximization and drag minimization of the aft foil.
- **Case 3:** Lift maximization of the fore foil.
- **Case 4:** Lift maximization and drag minimization of the fore foil.
- **Case 5:** Lift maximization and drag minimization of the aft foil, by retaining the same geometry for both foils.
- **Case 6:** Lift maximization and drag minimization of the fore foil, by retaining the same geometry for both foils.
- **Case 7:** Lift maximization and drag minimization of both foils, under the constraint of identical geometries.

- **Case 8:** Shape optimization of the aft foil to match its lift to the fore foil, using a morphing box applied to the aft geometry.
- **Case 9:** Shape optimization of the fore foil to match its lift to the aft foil, with modifications applied to the fore morphing box.

4.1 Case 1: Max C_l of the Aft Foil

The first optimization case represents the most fundamental and straightforward case within the series of studies, as it focuses on a single optimization objective at 9° common position angle: the lift force L generated by the aft hydrofoil, operating within the modified flow by the fore hydrofoil. By applying a controlled and gradual shape modification strategy, the optimization process was carried out of the cycles.

As a result, the final aft hydrofoil geometry achieved a 24.53% improvement in C_l compared to the baseline NACA4412 profile under tandem operation conditions, while the C_d has increased by 29.0 %. At the same time, the C_d of fore hydrofoil was reduced by 14.2 % and the C_l was increased by 1.68 %.

Figures 4.1 and 4.2 illustrate the initial and final positions of the morphing box control points, overlaid on the velocity contour plots, highlighting the localized geometric adjustments that contributed to the observed hydrodynamic performance enhancement.

Figure 4.1: Case 1: Velocity around the aft hydrofoil and its morphing box prior the optimization, at 9° common position angle.

In figures 4.5 and 4.6, the optimized hydrofoil geometry is presented along with its pressure distribution, both plotted against the CL. The results clearly indicate that the optimized profile tends to redistribute the surface pressure less linear along the chordwise (x-axis) direction, compared with the NACA4412 (baseline). This more widely distributed pressure distribution contributes positively to the generation of lift, as it enhances the overall pressure difference between the upper and lower surfaces of the foil, which is the primary mechanism behind lift production.

Figure 4.2: Case 1: Velocity around the aft hydrofoil and it's morphing box after the optimization, at 9° common position angle.

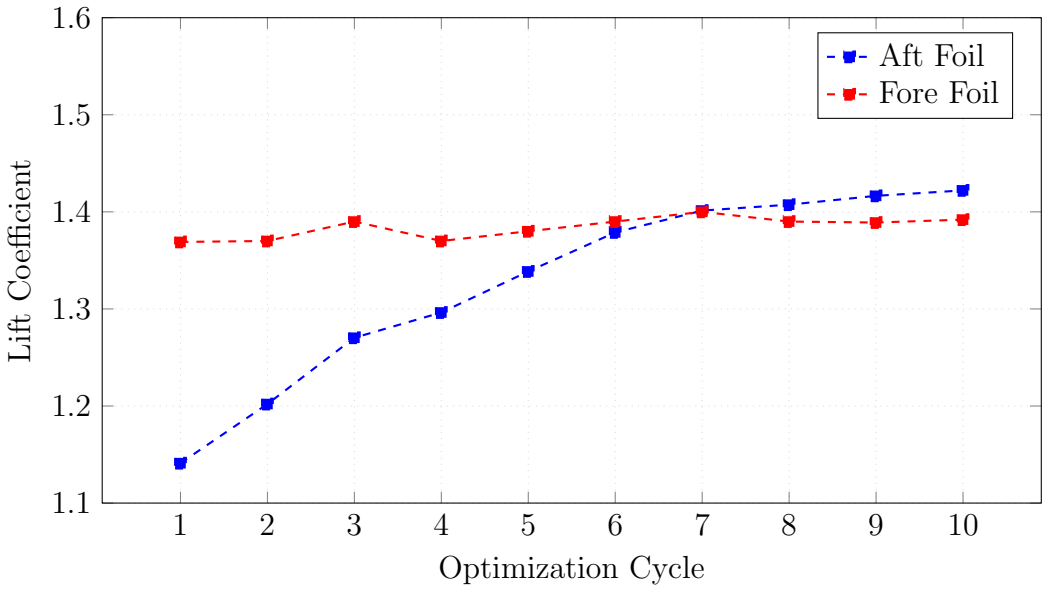

Figure 4.3: Case 1: Evolution of C_l of the fore and aft foils over 10 optimization cycles.

However, the geometry change also introduces a notable shift in the foil's maximum thickness location (the highest point along the y-axis), which has been displaced toward the mid-chord region. While this change supports the increase in lift, it simultaneously results in higher drag. This effect can be attributed to the increased frontal area and the associated pressure recovery challenges downstream of the maximum thickness. The outcome is consistent with hydrodynamic theory: when optimization is guided solely by lift maximization, without incorporating drag reduction as an additional objective or a constraint, the resulting geometry typically increases the camber and produces higher drag.

This case therefore illustrates the inherent trade-offs in single-objective optimization, where performance improvements in one parameter (lift) may

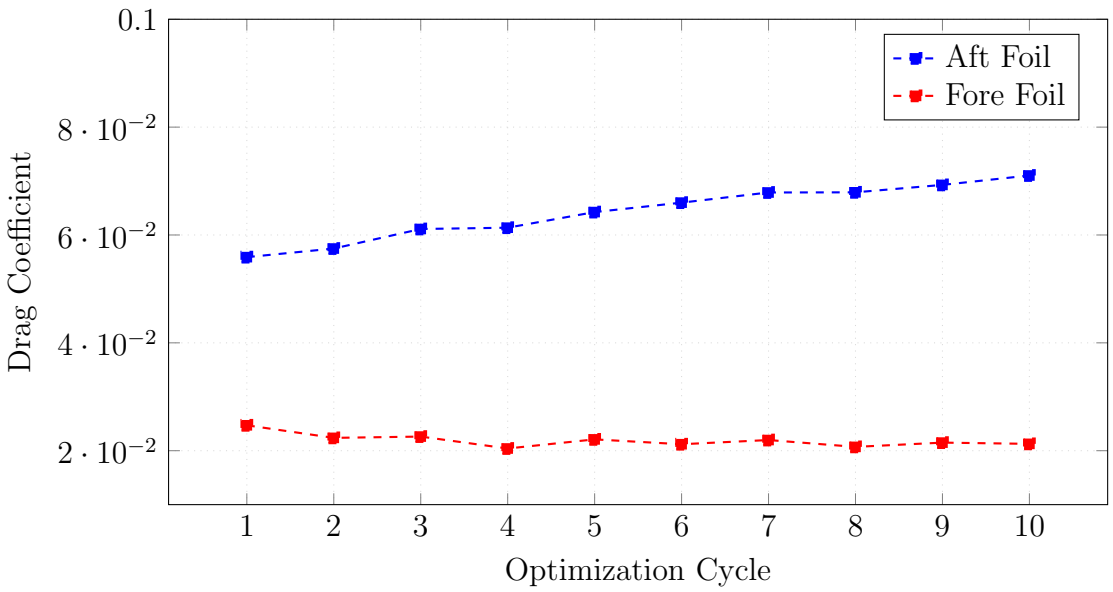

Figure 4.4: Case 1: Evolution of C_d of the fore and aft foils over 10 optimization cycles.

lead to compromises in another (drag). It also underscores the importance of adopting multi-objective optimization strategies, as similarly applied in the following cases, to achieve a balanced enhancement of lift-to-drag ratio, which is ultimately more relevant for hydrofoil efficiency in practical applications.

Additionally, the flow alterations by ShpO at aft foil has an impact on the coefficients of the fore hydrofoil, which sees a minor increase in lift but a notable reduction in its drag coefficient. This leads us to study the forces applied as a common object and not separately, as it will be presented in cases 5 to 7.

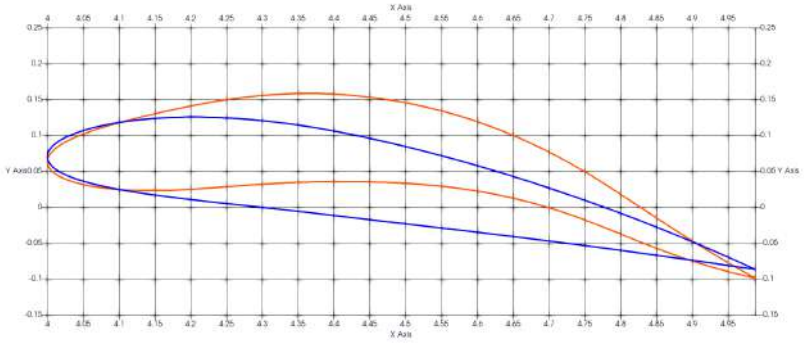

Figure 4.5: Case 1: Comparison of the aft hydrofoil geometry before and after the 10 optimization cycles, at 9° common position angle.

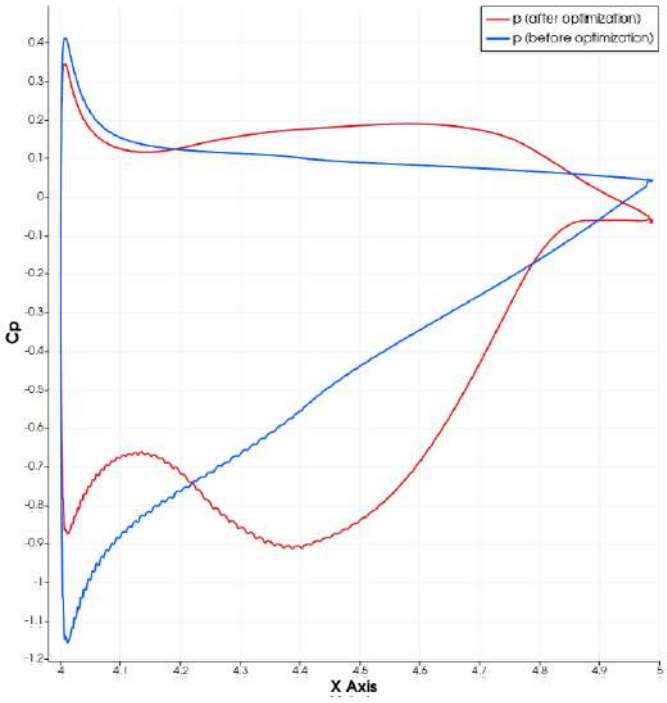

Figure 4.6: Case 1: The aft NACA4412 hydrofoil pressure distribution before and after ShpO to fore foil.

4.2 Case 2: Max C_l and Min C_d of the Aft Foil

The second optimization case follows the same gradient-based methodology as the first one but with the important distinction of incorporating drag minimization into the objective function. Specifically, the objective is formulated as a weighted sum of the lift and drag coefficients, with a weight of 1.0 applied to the lift term and 0.8 to the drag term ($J = 1.0 * L + 0.8 * D$). These weights are not normalized, thus the lift component continues to exert dominant influence over the optimization process. This application is closer to real life scenarios than Case 1, considering that the drag of a moving vehicle of any kind plays a significant role in its feasibility as a concept and its energy efficiency during actual operation.

Despite the dominance of the lift maximization term, the inclusion of drag introduces a subtle yet meaningful constraint that guides the geometry toward more physically realistic designs. This is evident when comparing the evolution of the lift coefficient across the two cases. The lift-only optimization achieves slightly higher lift values, but at the potential cost of geometric extremity or impracticality. In contrast, the lift-plus-drag optimization yields a slightly reduced lift improvement but benefits from improved geometric smoothness and aerodynamic plausibility.

Therefore, even with a modest contribution, the drag term in the objective function plays a critical role in regularizing the optimization and promoting balanced hydrodynamic performance.

By applying the above ShpO, the final aft hydrofoil geometry achieved a 24.66% improvement in lift coefficient compared to the baseline profile under tandem operation conditions, while the drag coefficient has increased by 25.45 % (compared to 29.0% of Case 1). At the same time, the C_d of fore hydrofoil was reduced by 11.21 % and the C_l was increased by 2.38 %.

Figures 4.7, 4.8, 4.9, 4.10 present the reduction in drag coefficient by applying lift and drag optimization targets on the hydrofoil, which sacrifices a minor lift portion (against Case 1) by adjusting the final geometry and pressure distribution.

Reviewing the results of case 2, we notice that incorporating a drag minimization target of a limited weight can lead to a minor change in the final geometry (compared to the lift maximization target of case 1) but also to 4% less drag and only 0.13% reduction at lift gains. This highlights the importance of multiple objectives optimization (in this case weighted under a single objective) in real life application and how modern tools or methodologies (e.g. continuous adjoint optimization combined with steepest decent)

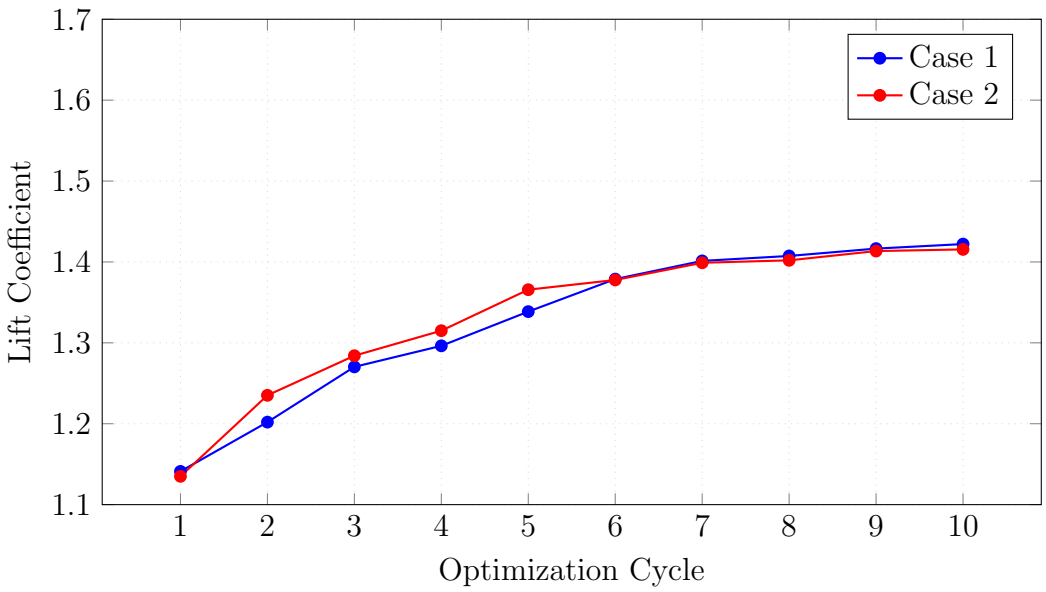

Figure 4.7: Case 2: Evolution of C_l over 10 optimization cycles.

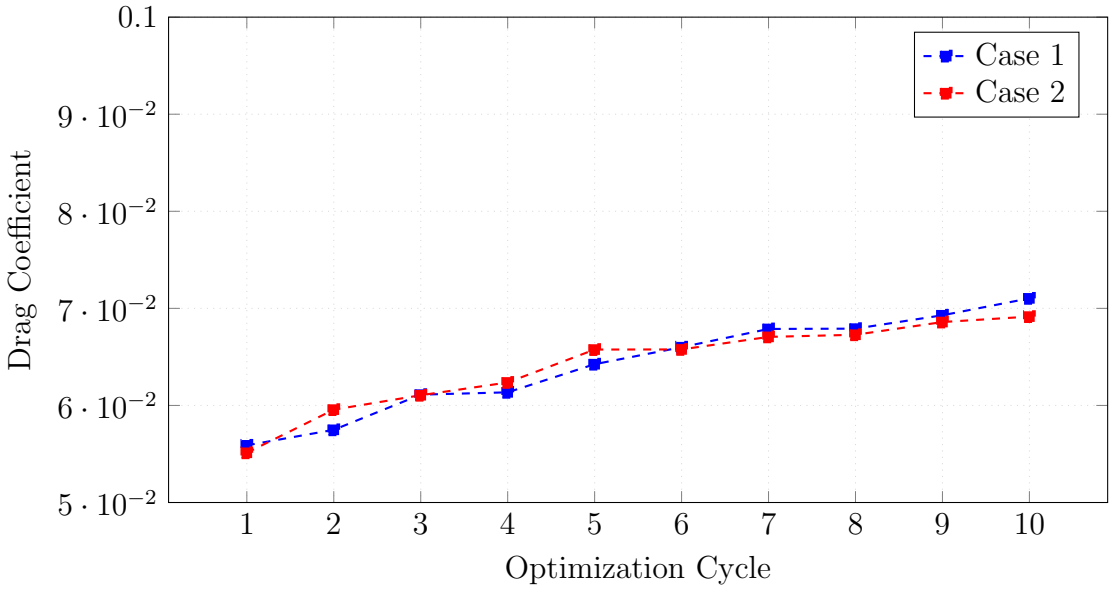

Figure 4.8: Case 2: Evolution of C_d over 10 optimization cycles.

can lead in highly improved results.

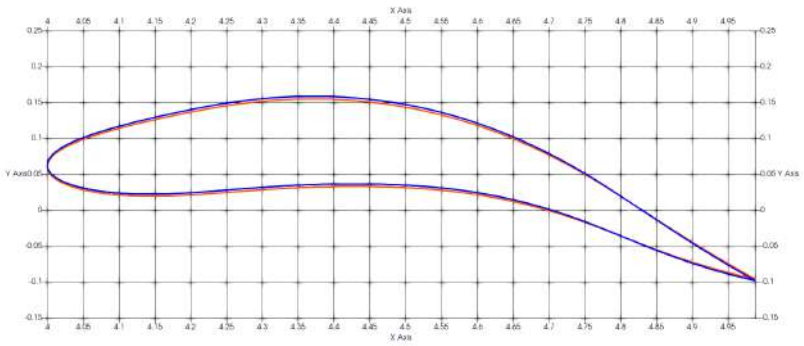

Figure 4.9: Case 2: Comparison of the geometry after the 10 optimization cycles of case 1 and 2 with lift and drag targets at aft foil, at 9° common position angle.

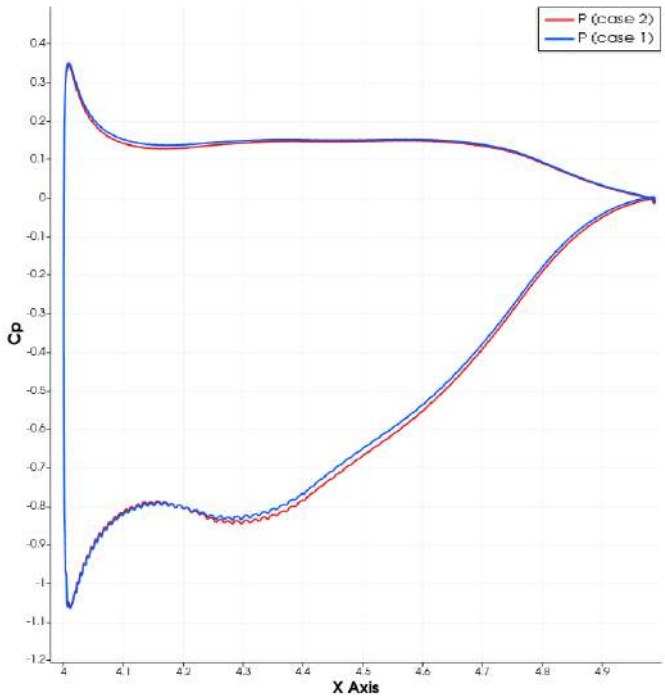

Figure 4.10: Case 2: Comparison of the C_p after the 10 optimization cycles of case 1 and 2.

4.3 Case 3: Max C_l of the Fore Foil

Building upon the established methodology of previous cases, the third optimization case was conducted to investigate the potential for performance enhancement of the forward hydrofoil by modifying its geometry. The objective function for this case was defined as the lift coefficient, C_l, generated solely by the fore foil, mirroring the single-objective approach employed in Case 1 for the aft foil. The optimization process was executed over 10 cycles, allowing the adjoint-based computation algorithm to converge towards a geometry that optimally fulfills this aerodynamic objective.

The results of this optimization endeavor demonstrated a successful improvement in the fore foil's performance. The final optimized geometry yielded a 16.33% increase in the lift coefficient compared to the baseline profile (NACA4412) operating under the same tandem conditions. This enhancement, however, was accompanied by a secondary effect: a 22.2% increase in the drag coefficient of the fore foil. A notable and indirect outcome was observed on the unmodified aft foil, which experienced a 5.21% increase in its own lift coefficient. This phenomenon underscores the strong and reciprocal hydrodynamic coupling inherent in tandem configurations, where a change in the fore foil's geometry and its resulting wake alters the inflow conditions for the aft foil.

When contextualized against the results of Cases 1 and 2, a critical insight emerges. The relative gain in lift for the fore foil (11.6%) is notably lower than the approximately 24.5% achieved for the aft foil. In a tandem arrangement, the fore foil benefits from interacting with clean, unperturbed freestream flow. Its baseline performance is already elevated due to hydrodynamic interference effects, leaving less margin for absolute improvement through shape optimization. In contrast, the aft foil operates within the velocity-deficient and turbulent wake of the fore foil, presenting a significantly larger design space for recovery and enhancement of its diminished performance.

In conclusion, Case 3 successfully demonstrates that optimization can effectively improve the lift characteristics of the fore hydrofoil. However, the results indicate that, for this specific tandem configuration, a greater potential for performance gain resides in optimizing the aft element. This is has importance for designers, suggesting that resource allocation for shape optimization should be prioritized based on the component operating in the most degraded flow environment to maximize the return on investment and achieve superior system-level performance.

To isolate the effect of the tandem configuration and provide a benchmark for the tandem optimization results, a complementary analysis is performed

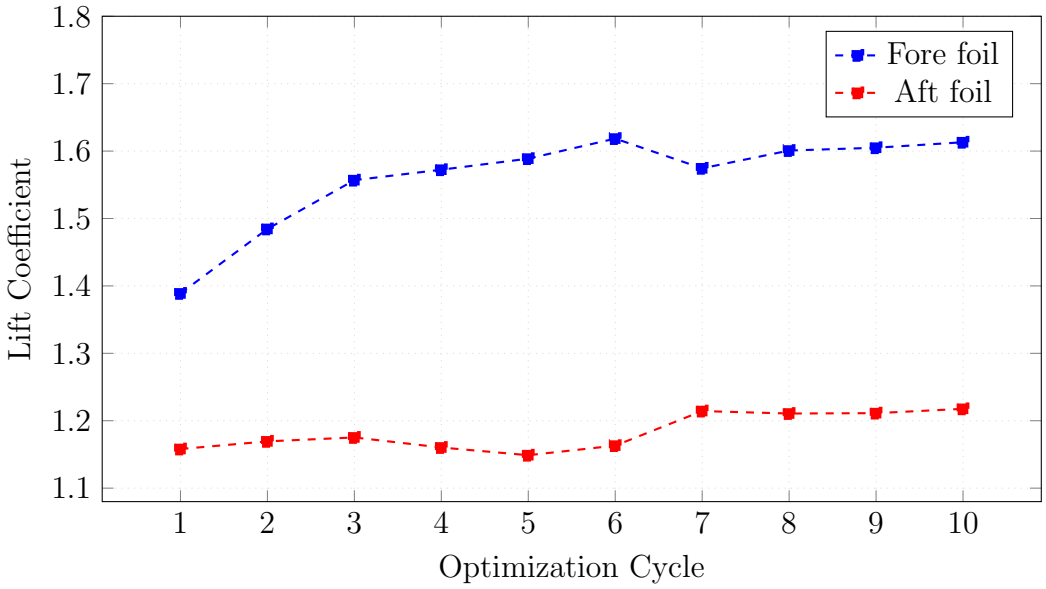

Figure 4.11: Case 3: Evolution of C_l over 10 optimization cycles.

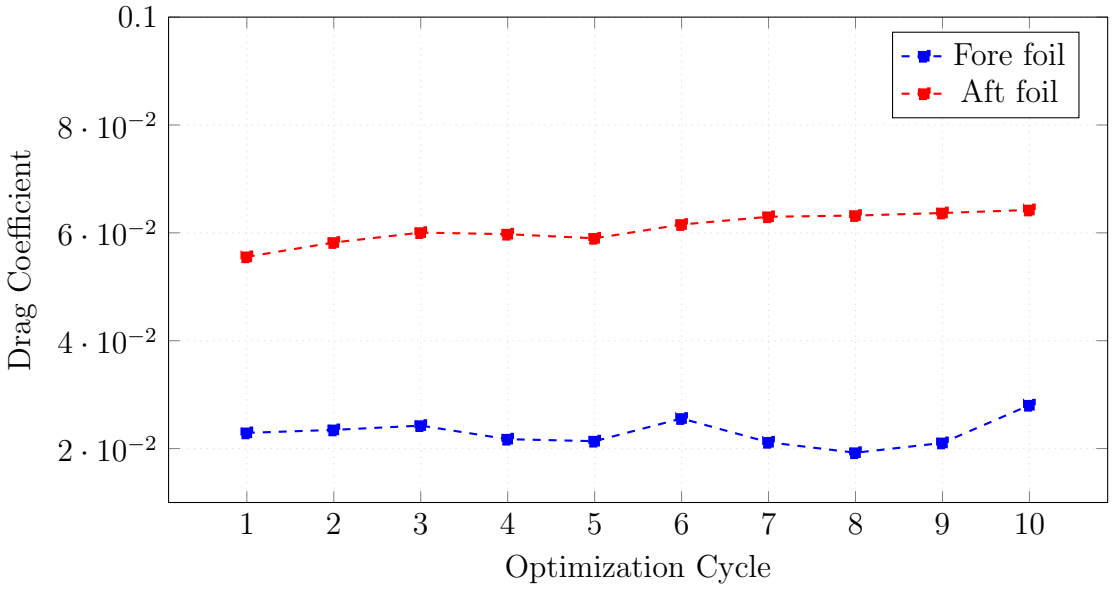

Figure 4.12: Case 3: Evolution of C_d over 10 optimization cycles.

on an isolated single foil NACA4412. The same lift maximization procedure is applied to the isolated hydrofoil in a free stream, which results to the performance trends and geometric changes shown in figures 4.15, 4.16, and 4.17. This comparative baseline allows for a clearer assessment of the perfor-

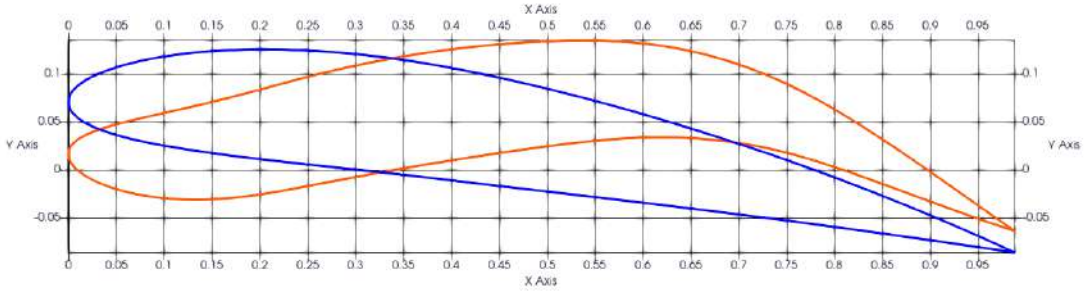

Figure 4.13: Case 3: Comparison of the geometry before and after the 10 optimization cycles applied at fore foil, at 9° common position angle.

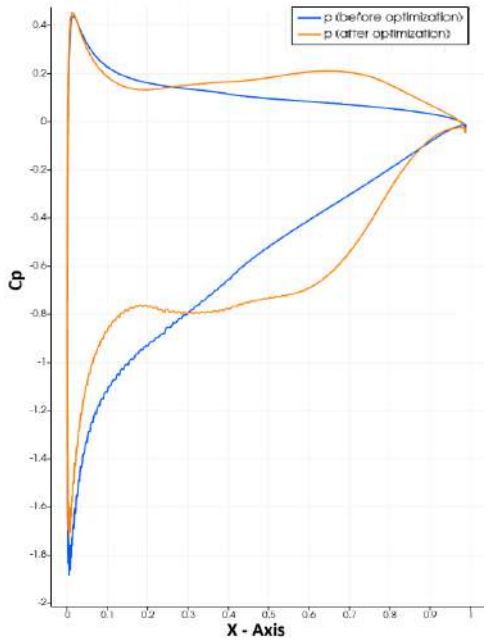

Figure 4.14: Case 3: Fore hydrofoil pressure distribution before and after 10 ShpO cycles.

mance gains attributable specifically to the hydrodynamic interaction within the tandem system. It is clear that the tandem hydrofoils cannot achieve the maximum lift under the same flow/angle parameters. This is the result of the modified flow generated by the tandem hydrofoils setup which limits their individual maximum lift potential.

Additionally, the final geometry of single foil optimization, has 92.8% higher drag coefficient compared to the final fore hydrofoil optimization under tandem operation.

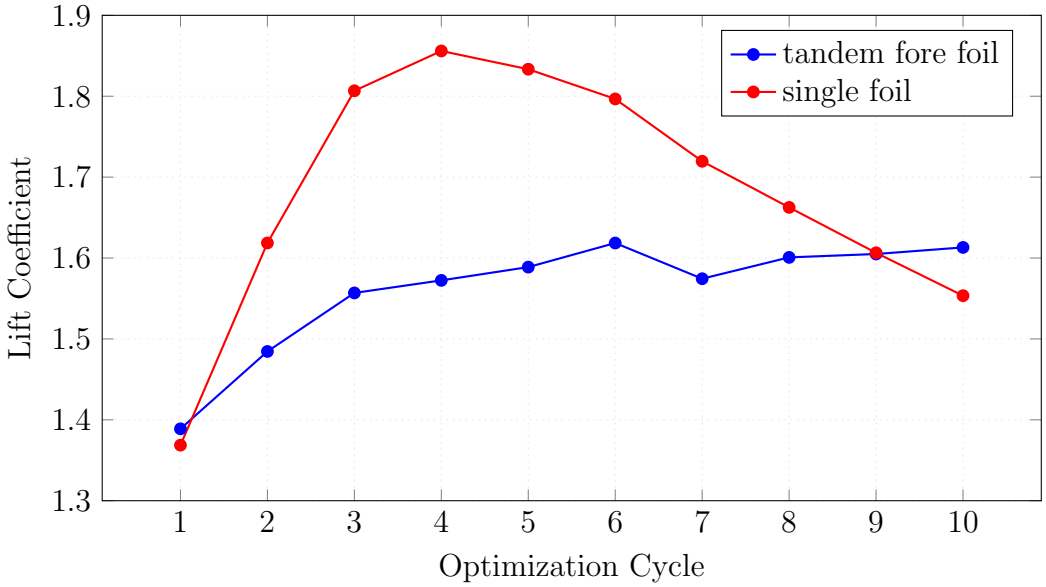

Figure 4.15: Case 3: Evolution of C_l over 10 optimization cycles.

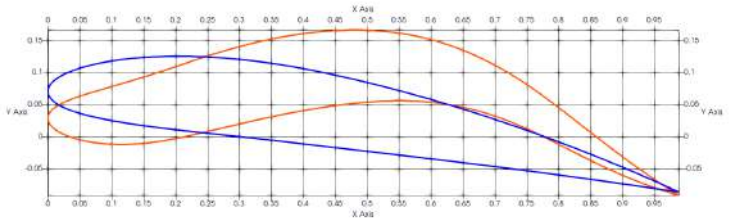

Figure 4.16: Case 3: Comparison of the geometry before and after the 10 optimization cycles applied at the foil without tandem setup, at 9° position angle.

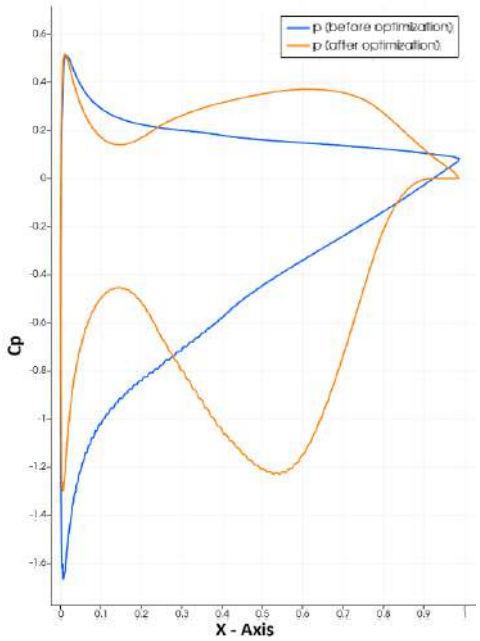

Figure 4.17: Case 3: NACA4412 hydrofoil pressure distribution before and after shape optimization applied to foil without tandem setup.

4.4 Case 4: Max C_l and Min C_d of the Fore Foil

Following the methodology of Case 2, this lift and drag weighted optimization targets the fore hydrofoil, aiming to simultaneously maximize its lift and minimize its drag. The objective function was formulated as a weighted sum of the lift and drag coefficients, with weights of 1.0 and 0.8, respectively, ensuring lift maximization remained the primary driver while incorporating drag as a regularizing constraint.

The optimization process, conducted over 10 cycles, yielded a significant 15.94% increase in the lift coefficient for the fore foil. Crucially, and in contrast to the single-objective approach of Case 3, this was achieved while successfully controlling the drag penalty. The drag coefficient of the case has been computed to be 6.74% less than the baseline. An additional, beneficial effect was observed: the lift of the unmodified aft hydrofoil increased by 1.39%.

A comparison between Case 3 and Case 4 reveals the critical importance of incorporating more targets during the optimization. By introducing drag into the objective function, the ShpO produced a final geometry that achieved a nearly identical lift coefficient (only 0.39% less than Case 3) with a drastically reduced drag coefficient (a 68.6% reduction). This result underscores that the optimization process is 'blind' to all performance metrics not specified in the objective function; a proper formulation is therefore essential for achieving physically meaningful and high-performing results.

Having completed the optimization cases 1 through 4, a comparative analysis of the final hydrodynamic coefficients is conducted to identify the most effective optimization strategy. The performance metrics for each case are summarized in Table 4.1.

Table 4.1: Comparison of final hydrodynamic performance coefficients for each optimization case, at 9° common position angle.

Case	**Description**	$C_{Lcombined}$	$C_{Dcombined}$	$C_{Lcombined}/C_{Dcombined}$
Case 1	Aft Foil Optimized	2.81	0.0920	30.54
Case 2	Aft Foil Optimized	2.80	0.0900	31.11
Case 3	Fore Foil Optimized	2.83	0.0920	30.76
Case 4	Fore Foil Optimized	2.81	0.0836	33.61

Analysis of the results leads to the conclusion that case 4 yields the most advantageous design. While case 3 achieves the highest lift coefficient ($C_l =$

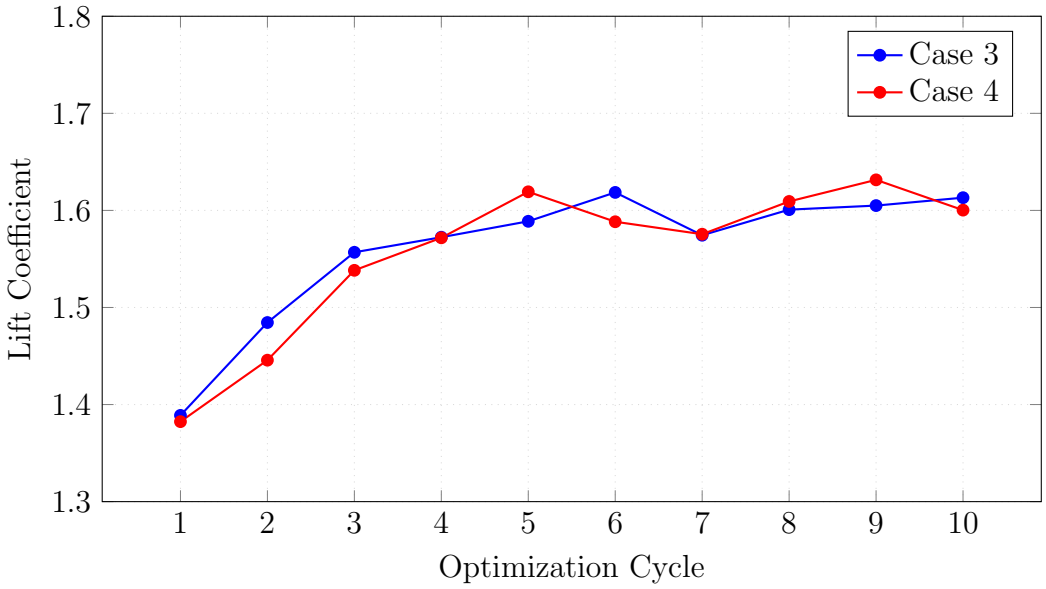

Figure 4.18: Case 4: Evolution of C_l over 10 optimization cycles.

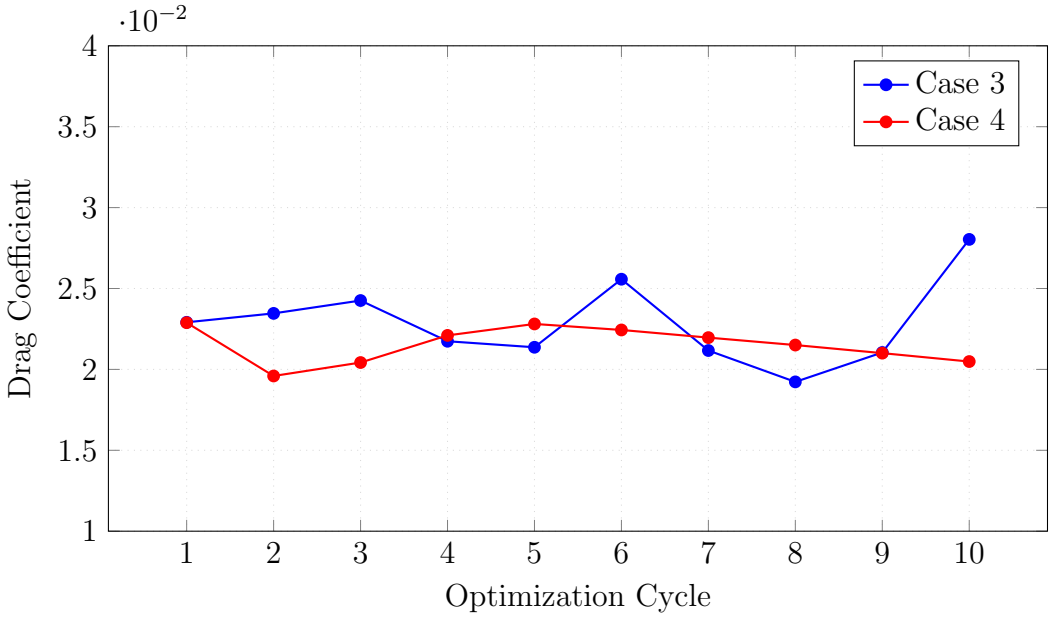

Figure 4.19: Case 4: Evolution of C_d over 10 optimization cycles.

2.83), it does so at a high drag penalty ($C_d = 0.092$). In contrast, case 4 produces a configuration with a competitively high lift coefficient ($C_l = 2.81$) and a dramatically lower drag coefficient ($C_d = 0.0836$). This represents a

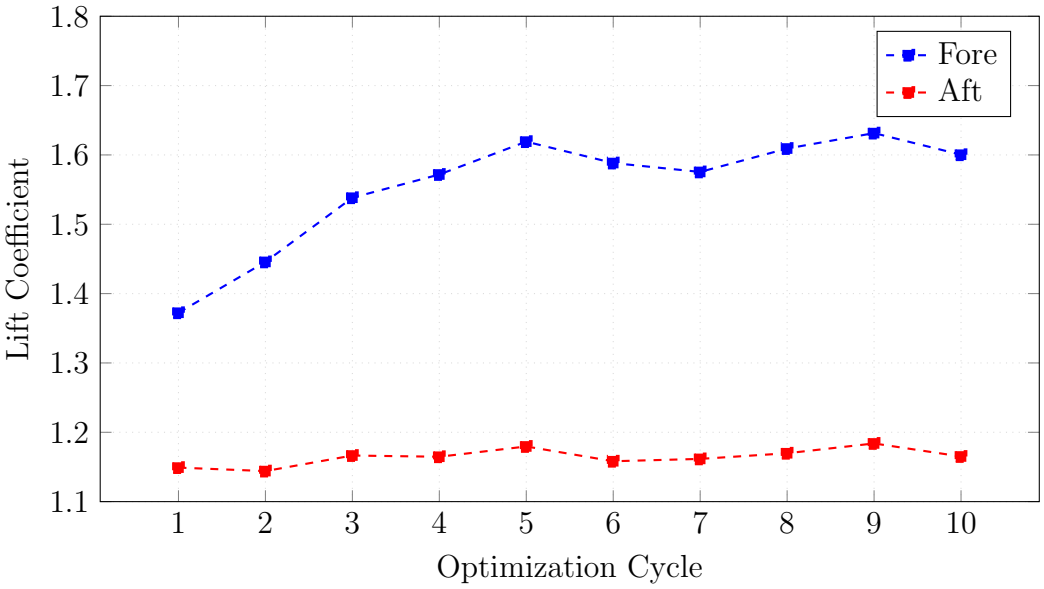

Figure 4.20: Case 4: Evolution of C_l for the fore and aft hydrofoils over 10 optimization cycles.

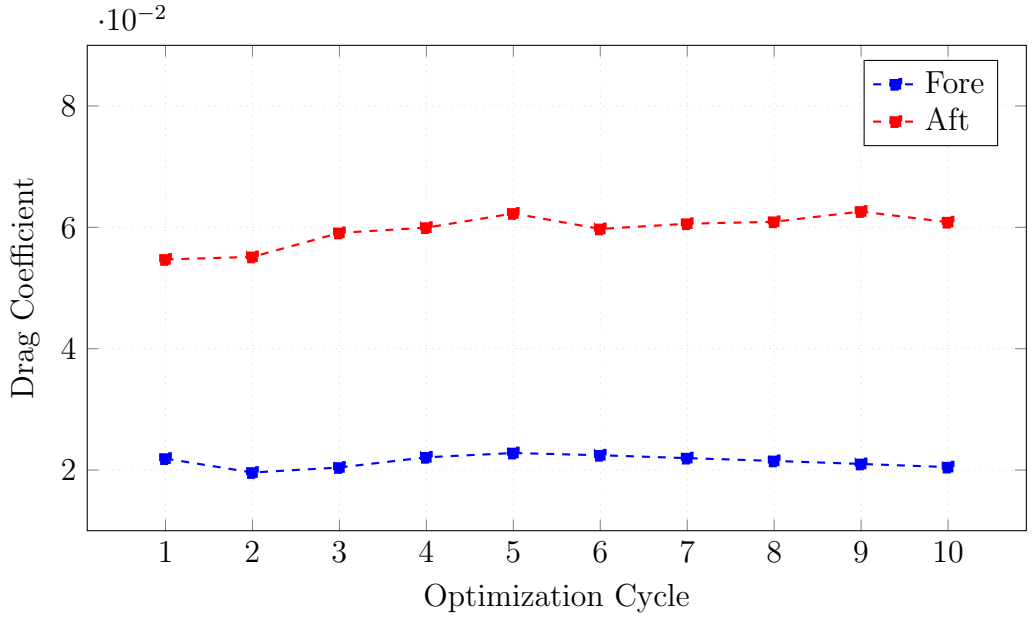

Figure 4.21: Case 4: Evolution of C_d for the fore and aft hydrofoils over 10 optimization cycles.

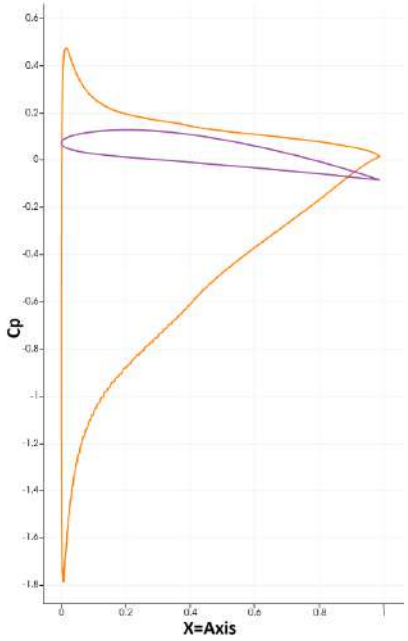

Figure 4.22: Case 4: Fore NACA4412 and it's pressure distribution in tandem mode before optimization, at 9° common position angle.

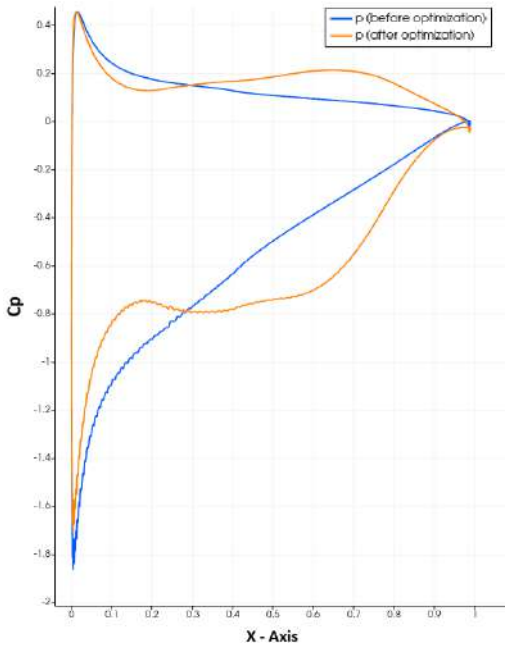

Figure 4.23: Case 4: Pressure distribution before and after 10 optimization cycles.

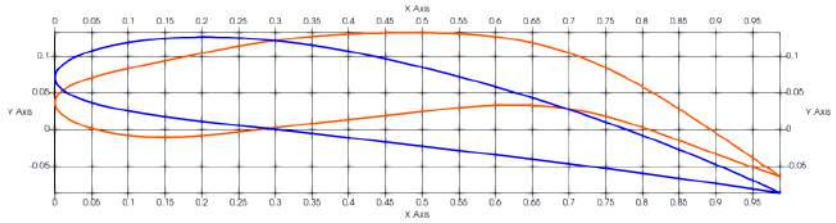

Figure 4.24: Case 4: Optimized and original geometry of fore foil, at 9° common position angle.

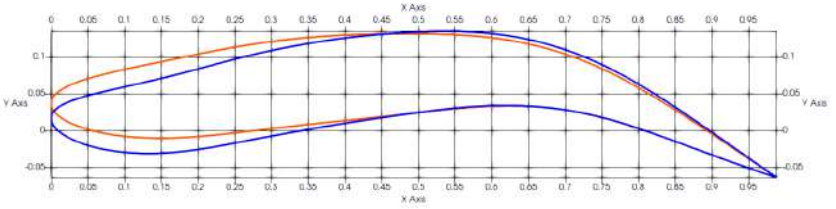

Figure 4.25: Case 4: Comparison of the optimized fore hydrofoil with (orange) and without (blue) drag as a target, at 9° common position angle.

drag reduction of approximately 9.1% compared to both the baseline (case 1) and case 3.

Consequently, the lift-to-drag ratio (C_L/C_D), a critical metric for efficiency, is highest in case 4. Therefore, if the design constraint is to modify only a single foil starting from a common geometry (NACA4412), optimizing the fore foil (and not the aft, similarly to case 4) is unequivocally the optimal strategy. This result underscores the paramount importance of the fore foil in managing the flow field and setting the inflow conditions for the aft element. An optimized fore foil not only generates favorable pressures itself but also effectively conditions the flow to minimize the drag and maximize the lift contribution of the unmodified aft foil.

4.5 Case 5: Max C_l and Min C_d of Aft Foil with identical shapes

This case introduces a key practical engineering constraint: part commonality. The optimization objective was defined as a weighted sum targeting lift maximization and drag minimization specifically for the aft hydrofoil ($J = 1.0 * L + 0.8 * D$). The constraint applied was that the resulting optimized geometry must be identical for both the fore and aft foils. This approach tests the viability of deriving a single, universally optimal shape from the component operating in the most degraded flow regime (the aft foil) and applying it to the entire system.

The optimization process is executed for 10 cycles. The final shared geometry yielded a significant (17.13%) increase in lift for the aft foil and a 17.40% increase for the fore foil. Regarding drag, the aft foil experienced a 24.86% increase, while the fore foil saw a 22.41% reduction. This divergence highlights the inherent compromise: a shape optimized for the wake-affected aft foil, when applied to the fore foil, creates a geometry that is overly aggressive for the clean inflow, leading to higher pressure drag on the aft component while beneficially accelerating flow over the fore component. The collective system performance showed a 17.46% increase in total lift against an 10.73% increase in total drag. In figure 4.26, the highest weight function maximization point is achieved at optimization cycle 8 of the algorithm. Additionally, in Figures 4.27 and 4.28, while the lift of both foils is increasing with similar movement and direction, the aft foil drag is reducing. Therefore, the aft foil is at the same time gaining at both force coefficients.

This case demonstrates that enforcing at both foils identical shapes based on the aft foil's optimization can generate substantial system-wide lift im-

provements. However, the trade-off is a significant increase in drag on the aft foil, underscoring the performance cost incurred when prioritizing manufacturing simplicity over bespoke hydrodynamic tailoring.

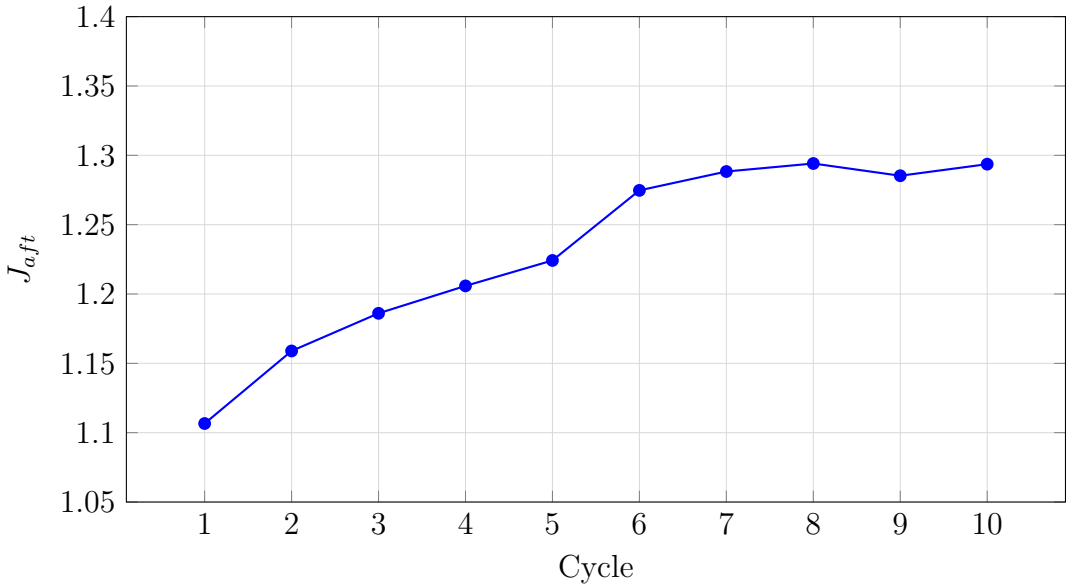

Figure 4.26: Case 5: evolution of J_{aft} over 10 optimization cycles.

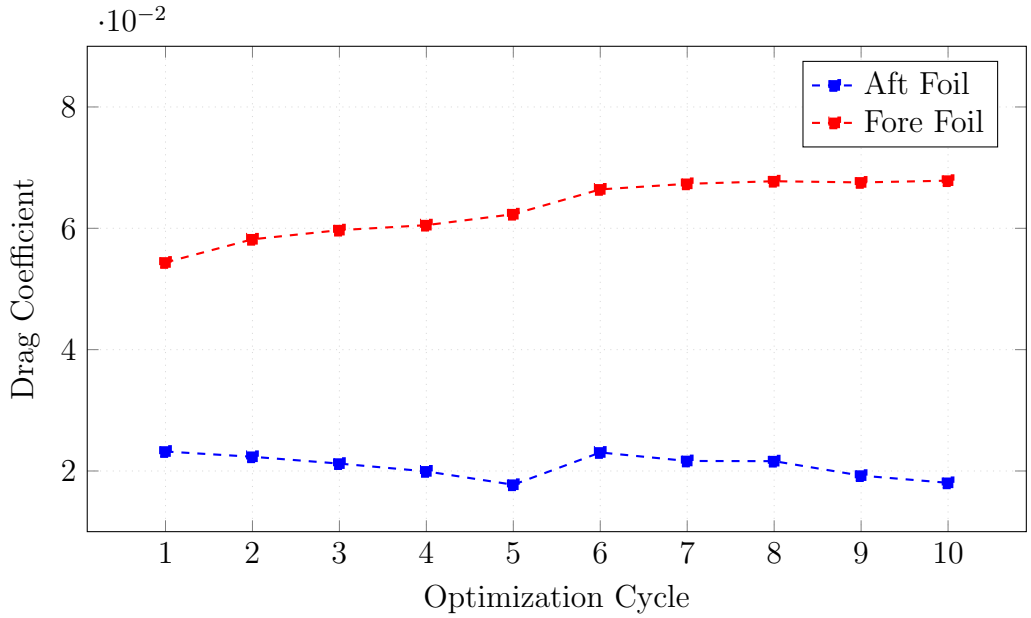

Figure 4.27: Case 5: evolution of C_d over 10 optimization cycles.

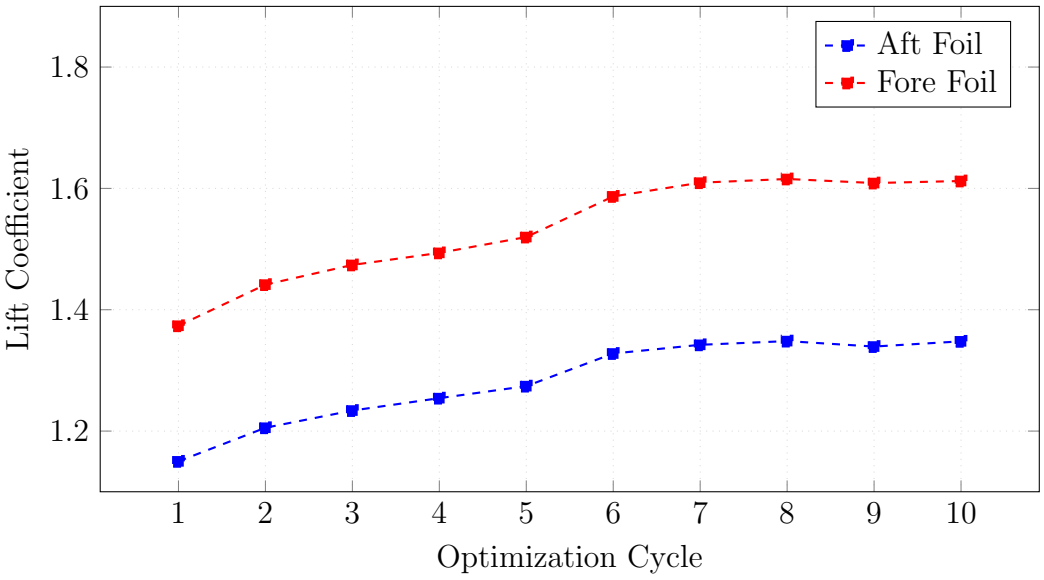

Figure 4.28: Case 5: evolution of C_l over 10 optimization cycles.

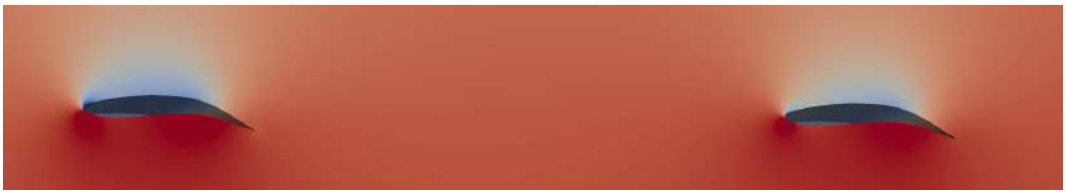

Figure 4.29: Case 5: The commonly shared optimized geometries and their pressure distribution in tandem mode, at 9° common position angle.

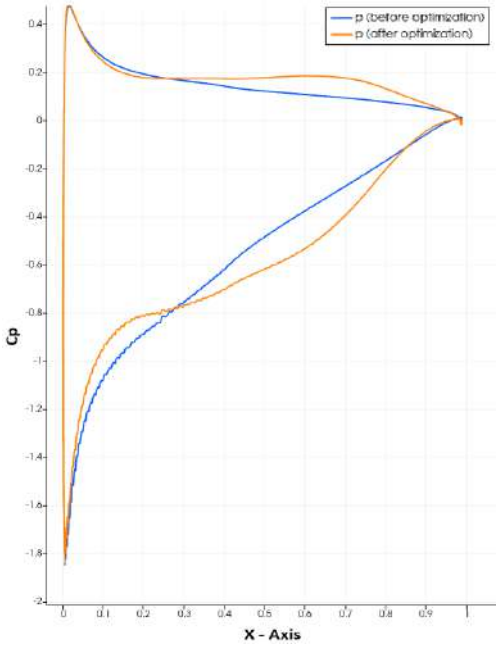

Figure 4.30: Case 5: Pressure distribution at the fore foil, before and after the 10 optimization cycles applied at the aft foil while maintaining identical geometries, at 9° common position angle.

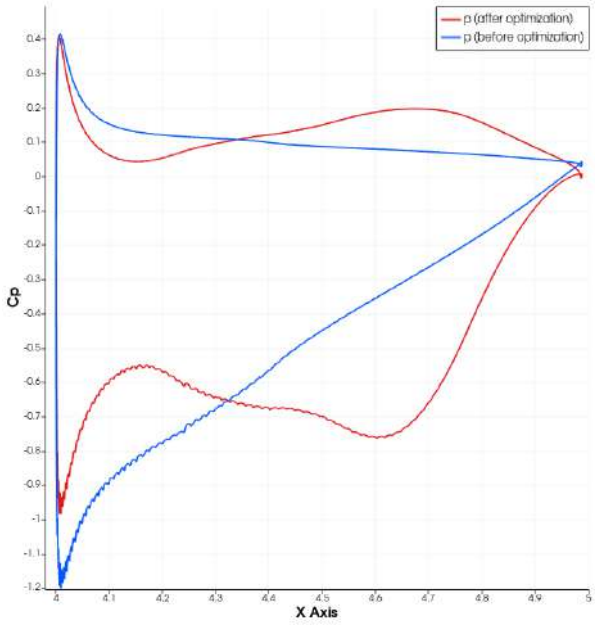

Figure 4.31: Case 5: Pressure distribution at the aft foil before and after the 10 optimization cycles.

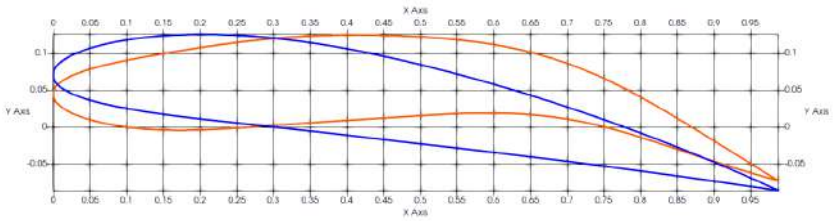

Figure 4.32: Case 5: Aft foil optimized and original geometry, at 9° common position angle.

4.6 Case 6: Max C_l and Min C_d of the Fore Foil with identical shapes

Case 6 investigates the inverse of the previous case, exploring the system-wide effects of deriving a identical shapes from the fore hydrofoil's optimization. The objective function remained a weighted sum for lift and drag, but was now applied solely to the fore foil, with the identical constraint that both foils must share the resulting shape. This tests a strategy where the geometry is optimized for the component in clean flow and imposed on the one within the wake.

The optimization was run for 10 cycles. The resulting performance trends, visible in figures 4.33 and 4.34, indicate a different compromise. A geometry tailored for the high-performance fore foil, when applied to the aft foil, is too conservative for the recovery of lift in a wake. Typically, this leads to muted performance gains for the aft foil, as its shape is not aggressive enough to effectively overcome the velocity deficit it experiences. Consequently, the aft drag is increasing (in contrast to case 5) and the overall system drag is more compared to Case 5. Similarly with case 4, by applying ShpO to the fore foil we can achieve better lift increase and thus, the combined lift of this case is better than optimizing the aft foil with identical shapes.

The maximum lift of this case is achieved at optimization cycle 9, where the collective system performance showed a 18.70% increase in total lift against an 13.44% increase in total drag. Specifically for each foil, for the fore lift increased by 18.93% and drag by 14.65%. For aft foil, the lift increased by 18.34% and drag 25.59%.

The results of Case 6 highlight that a identical shapes strategy driven by the fore foil's objectives is more effective for overall system lift enhancement.

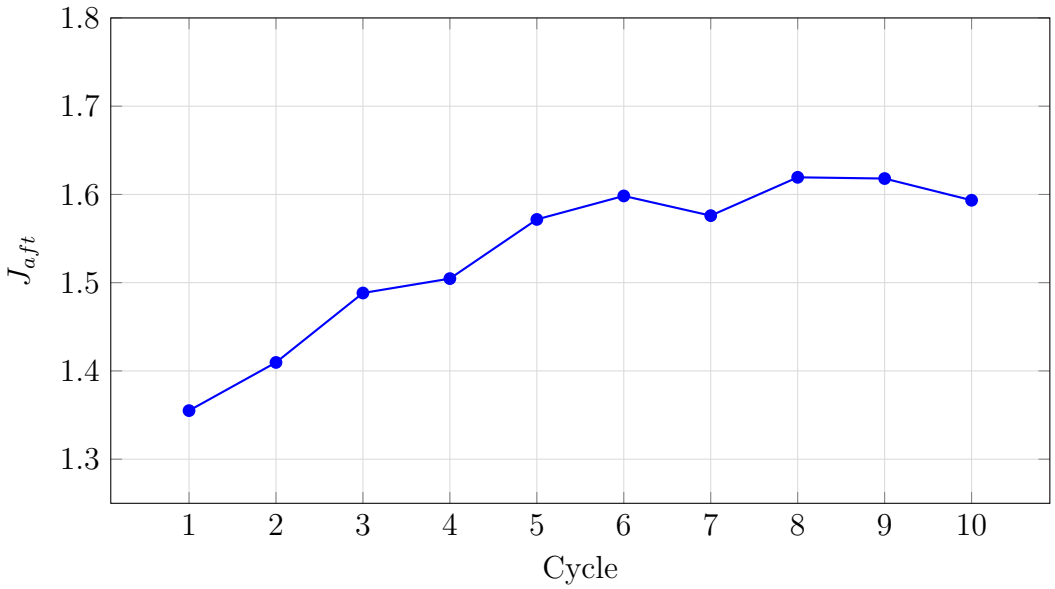

Figure 4.33: Case 6: Evolution of J_{aft} maximization over 10 optimization cycles.

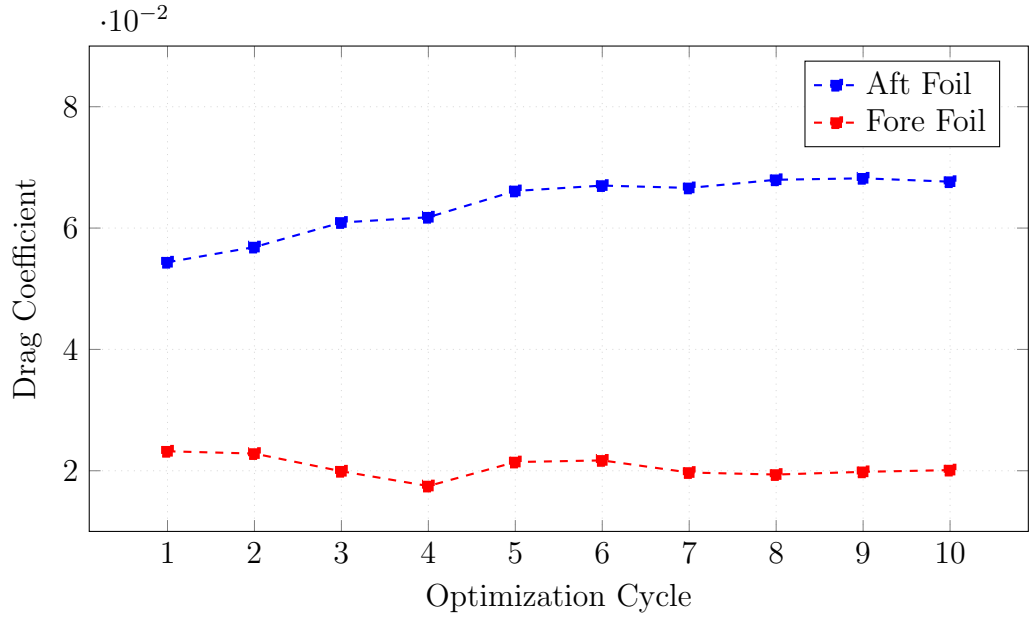

Figure 4.34: Case 6: Evolution of C_d over 10 optimization cycles.

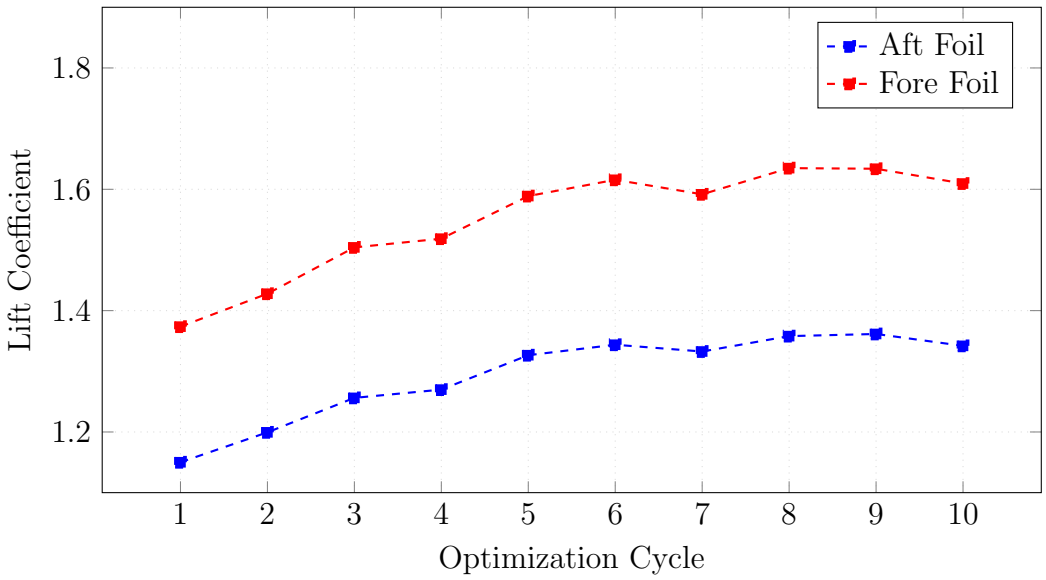

Figure 4.35: Case 6: Evolution of C_l over 10 optimization cycles.

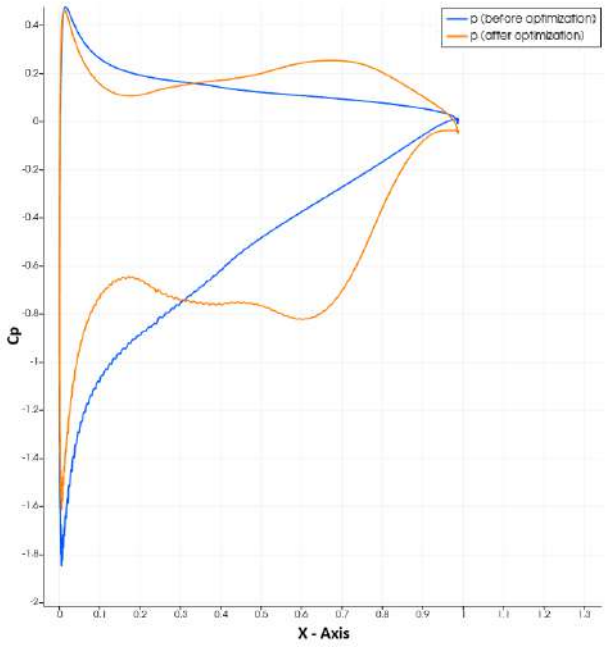

Figure 4.36: Case 6: Fore foil pressure distribution before and after 10 optimization cycles.

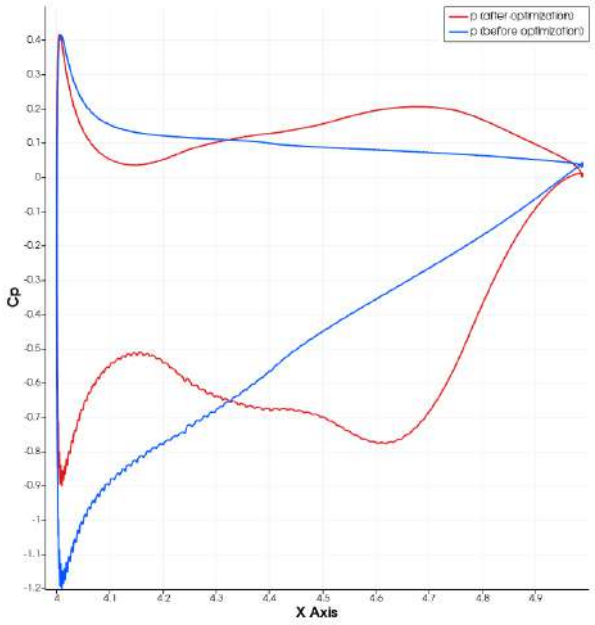

Figure 4.37: Case 6: Aft foil pressure distribution before and after 10 optimization cycles.

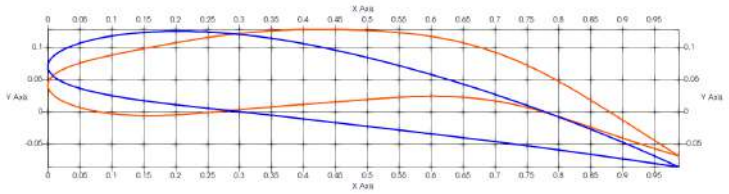

Figure 4.38: Case 6: Fore foil optimized shared geometry and the original NACA4412 geometry, at 9° common position angle.

4.7 Case 7: Max C_l and Min C_d at Both Foils with identical shapes

From the experience gained by the previous cases, we notice that while the optimization targets remain at just on one of the two examined hydrofoils (fore or aft), both of them are more or less affected by any changes on the flow, even if the shape of one foil remains unchanged (cases 1 to 4). Thus, we conclude that on any shape or object where the common lift or drag coefficients are the mostly interesting factors, all involved geometries will need to be optimized at the same time, with common targets. On this case, both the fore and aft hydrofoil shapes are incorporated on the two common weighted optimization objectives, which are the lift maximization (weight 1.0) and drag minimization (weight 0.8), with their weights not normalized. The computed derivatives of both foils are used to adjust and optimize their shared geometry. Thus, the sum of the coefficients of both foils is monitored at each optimization circle and the updated geometry is commonly applied at both hydrofoils. This, results not only in shared identical shapes but also at an optimal lift force generation through their interaction. At figure 4.40 we can also notice that the trend in fore and aft hydrofoils remains the same proportionally for each shape during ShpO.

As expected, with this approach we can achieve the best overall coefficients along case 6, compared to single foil optimization (fore or aft) and case 5. The above proves that the optimization of fore foil (as it is part of both cases 6 and 7) is the most important factor in achieving the best lift maximization.

The maximum lift of this case is achieved at optimization cycle 6, where the collective system performance showed a 17.78% increase in total lift against an 17.10% increase in total drag. Specifically for each foil, at the fore lift increased by 17.68% and drag by 10.72%. At aft foil, the lift increased by 18.34% and drag 20.51%.

Having completed the optimization cases 5 through 7, a comparative analysis of the final hydrodynamic coefficients is conducted to identify the most effective optimization strategy containing both foils with shared geometry. The performance metrics for each case are summarized in Table 4.2.

Analysis of the results leads to the conclusion that case 6 and 7 yields the most advantageous design regarding the lift maximization target, which is expected if we consider that these cases optimize the fore foil which can achieve the highest lift. While these cases showed the highest lift coefficient ($C_l = 2.99$), they do so at a high drag penalty ($C_d = 0.088$). In contrast, case 5 produces a configuration with a competitively high lift co-

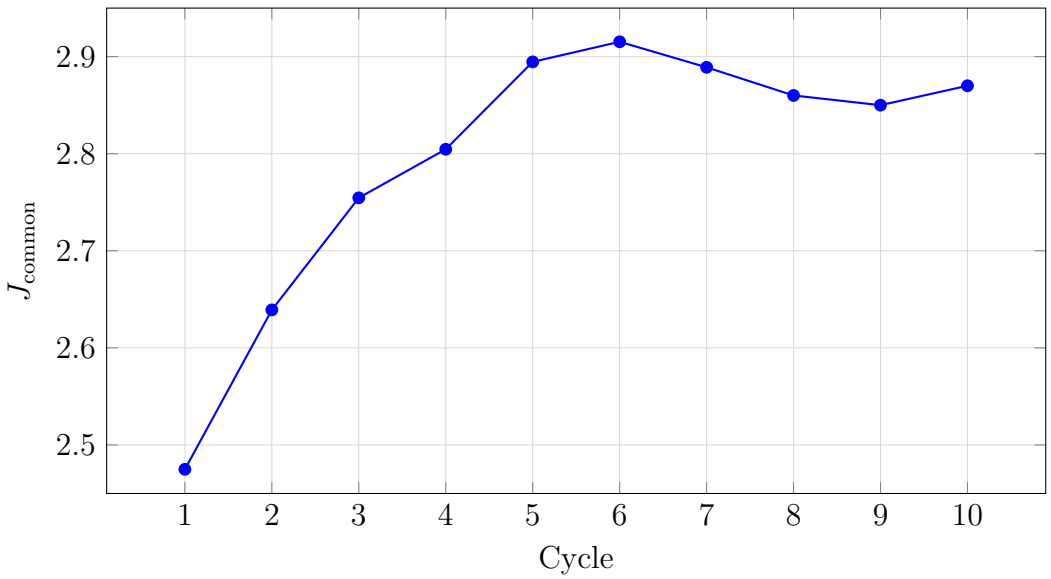

Figure 4.39: Case 7: Evolution of J_{common} over 10 optimization cycles.

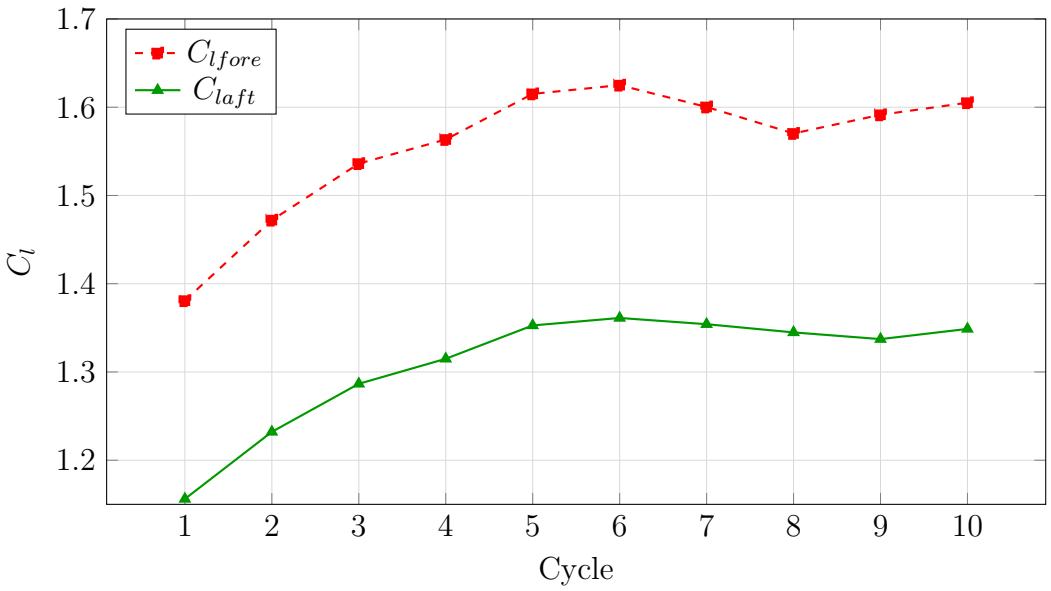

Figure 4.40: Case 7: Evolution of C_{lfore} and C_{laft} over 10 optimization cycles.

efficient ($C_l = 2.96$) and a notable lower drag coefficient ($C_d = 0.085$). Additionally, case 5 produces the highest Cl/Cd ratio among all options with $C_{Lcombined}/C_{Dcombined} = 34.82$. Although the common force coefficients are very similar for cases 6 and 7, their final geometries are not alike, as can be

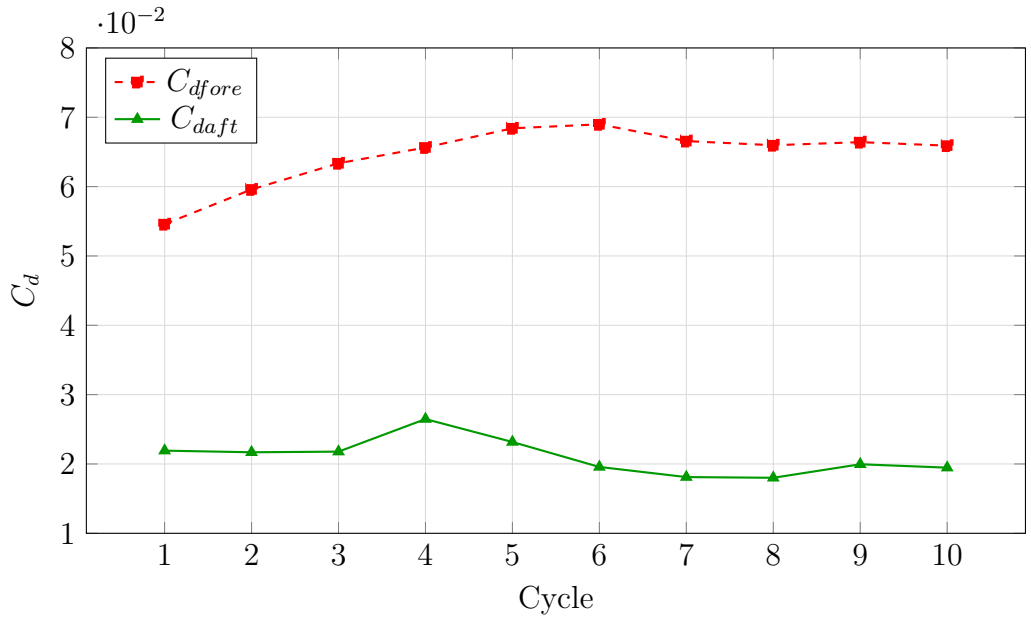

Figure 4.41: Case 7: Evolution of C_{dfore} and C_{daft} over 10 optimization cycles.

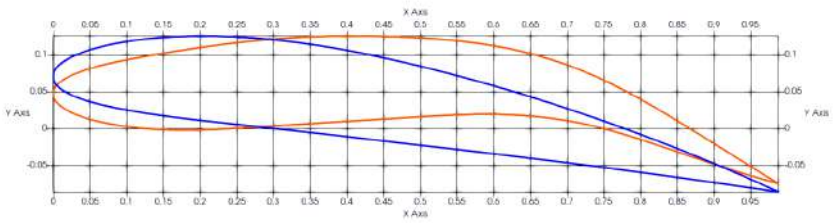

Figure 4.42: Case 7: Optimized identical shapes on both foils and NACA4412, at 9° common position angle.

observed at figure 4.46. This is expected considering that they both achieved the maximum lift but under different sensitivities, thus and different ShpO. Additionally, this implies that the final geometries individually will generate different forces (fore and aft) but their sum will be the same.

Figure 4.43: Case 7: Pressure distribution around the optimized common geometries of fore and aft hydrofoils, at 9° common position angle.

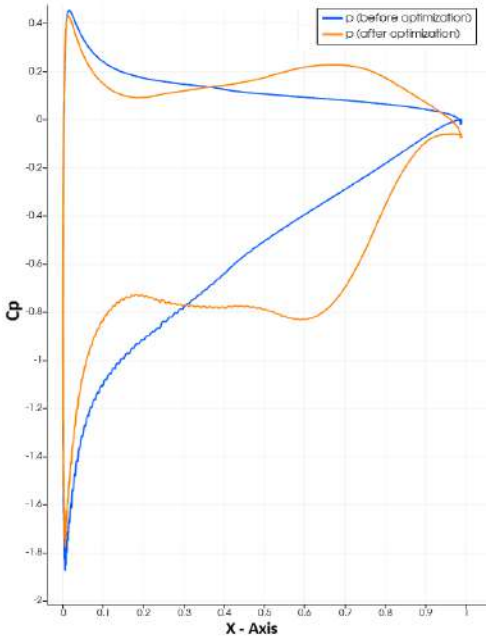

Figure 4.44: Case 7: Pressure distribution of fore foil before and after common ShpO, at 9° common position angle.

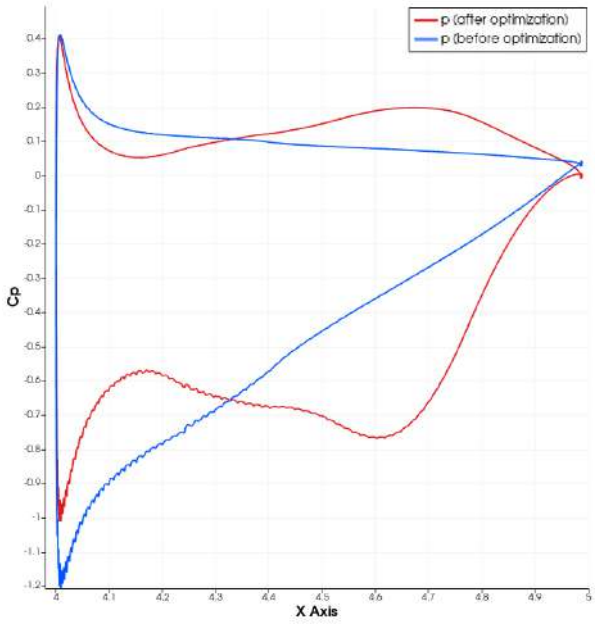

Figure 4.45: Case 7: Pressure distribution of aft foil before and after common ShpO, at 9° common position angle.

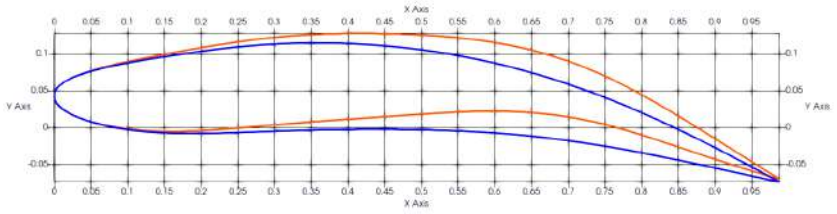

Figure 4.46: Case 7: Comparison of optimal geometry of case 6 (blue) and 7 (orange), at 9° common position angle.

Table 4.2: Comparison of final aerodynamic performance coefficients for each optimization case, at 9° common position angle.

Case	**Description**	$C_{Lcombined}$	$\mathbf{C_{D,\text{total}}}$	$C_{Lcombined}/C_{Dcombined}$
Case 5	Aft foil Shpo applied to both	2.96	0.085	34.82
Case 6	Fore foil Shpo applied to both	2.99	0.088	33.97
Case 7	Common ShpO applied to both	2.99	0.088	33.97

4.8 Case 8: match the C_l of the aft foil to the C_l of fore foil, by adjusting the aft

A common requirement in the design of multi-component lifting systems, such as tandem hydrofoil configurations, is the balanced distribution of hydrodynamic loads. An imbalance in lift between the fore and aft foils can lead to suboptimal performance, compromised stability, and increased structural loads. The two next cases investigates the application of adjoint-based shape optimization to tailor the geometry of the aft or fore hydrofoil such that its lift coefficient matches that generated by the other foil in tandem operation.

On the subject case, the aft hydrofoil will be optimized with a given target at lift coefficient (C_{lfore}) of

$$C_{laft} = C_{lfore} = 1.38 \tag{4.1}$$

while the drag term, with a weight of 0.8, acts as a regularizing constraint to prevent the emergence of geometrically extreme or drag-prolific solutions.

The optimization process is conducted over four cycles, with shape modifications confined to the aft hydrofoil via a dedicated morphing box. The results, illustrated in Figures 4.47 through 4.48, confirm the effectiveness of the approach. The lift coefficient of the aft foil successfully increased towards the target value of 1.38. To achieve this, the optimization algorithm introduced a greater camber to the aft hydrofoil geometry, enhancing its lift-generating capability. The pressure distribution around the optimized foil (Figure 4.50) shows a more uniform pressure field on the high-pressure side (lower surface), indicative of a more efficient pressure recovery and lift generation.

As anticipated, the increase in camber and lift was accompanied by a rise in the drag coefficient, a typical trade-off in hydrodynamic design. However, the inclusion of the drag minimization term in the objective function mitigated this increase, ensuring a more balanced performance improvement than a pure lift-maximization strategy would yield.

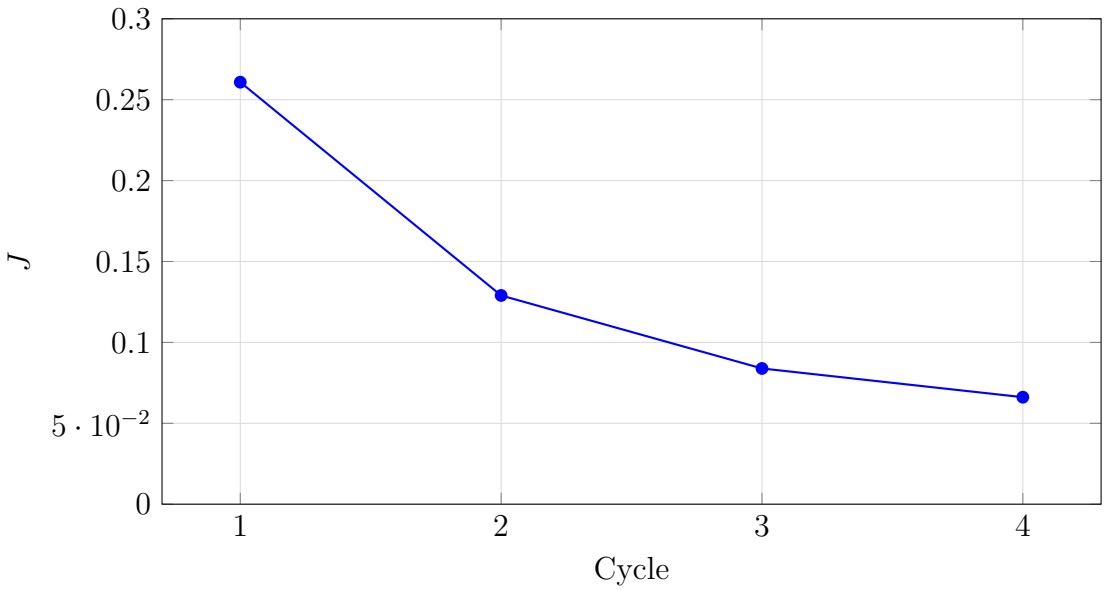

Figure 4.47: Case 8: Evolution of J over 4 optimization cycles.

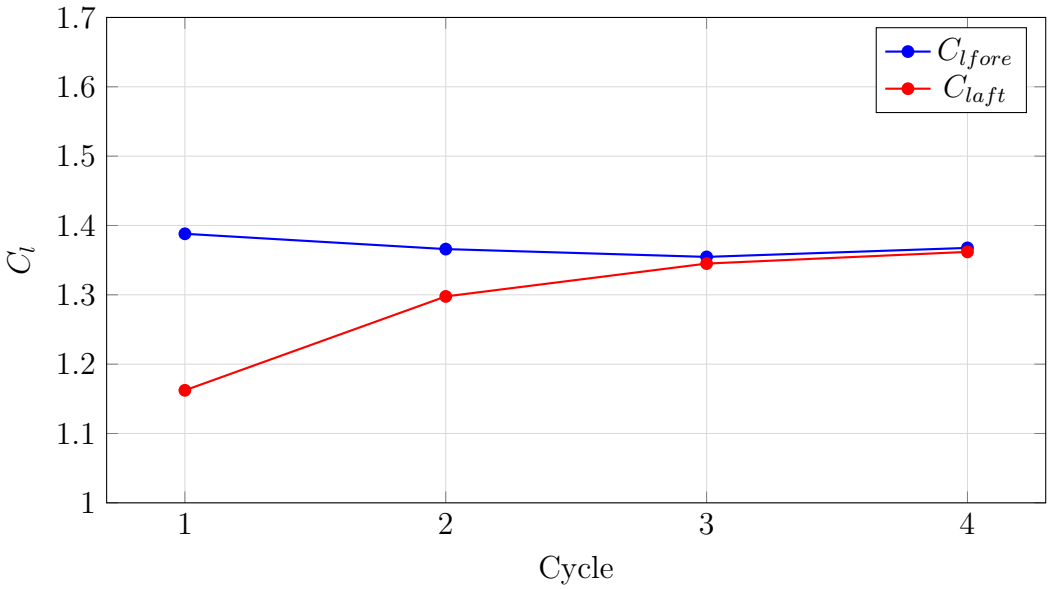

Figure 4.48: Case 8: Evolution of C_{lfore} and C_{laft} over optimization 4 cycles.

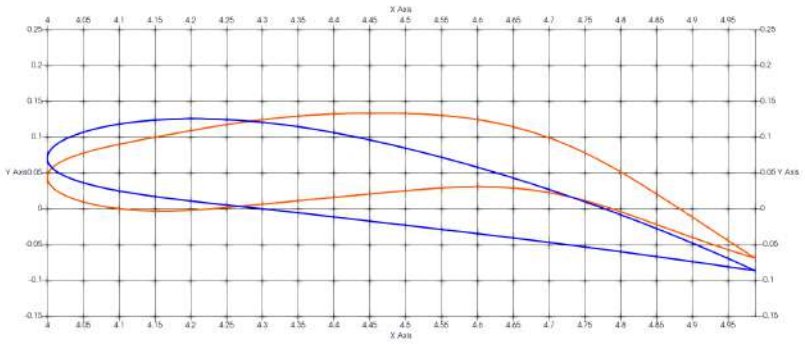

Figure 4.49: Case 8: Geometry before and after optimization for the aft hydrofoil, at 9° common position angle.

Figure 4.50: Case 8: Pressure distribution around the optimized aft geometry and the original fore hydrofoil, at 9° common position angle.

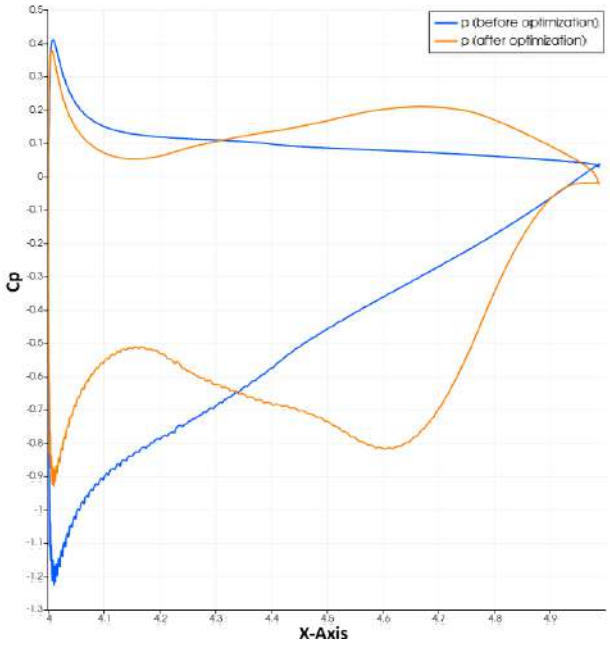

Figure 4.51: Case 8: Aft foil pressure distribution before and after the 4 optimization cycles.

4.9 Case 9: match the C_l of fore foil to the C_l of aft, by adjusting the fore

The inverse scenario to Case 8 is equally relevant in practical design. Situations may arise where it is desirable to reduce the load on the forward component to match the inherently lower lift capability of the aft foil operating in its wake. This could be motivated by structural constraints, stability requirements, or a specific design philosophy aiming for symmetric load distribution. This case explores the optimization of the fore hydrofoil to reduce its lift coefficient and match that of the baseline aft foil.

On this case the fore hydrofoil will be optimized with a target at lift coefficient of

$$C_{lfore} = C_{laft} = 1.18 \tag{4.2}$$

and while also keeping the drag target at reduced weight ($J = 1.0*L+0.8*D$).

The optimization was executed over five cycles, applying geometric modifications only to the fore hydrofoil. The results, presented in Figures 4.51 to 4.53, show a successful reduction in the fore foil's lift coefficient towards the desired value. To achieve this reduction, the optimization process yielded a geometry with reduced camber compared to the baseline NACA 4412 profile. The corresponding pressure distribution (Figure 4.53) exhibits a less pronounced suction peak on the upper surface and a more uniform pressure on the lower surface, resulting in a smaller overall pressure differential and hence, lower lift.

Concurrently, the reduction in camber and lift led to a decrease in the pressure drag component, resulting in a lower drag coefficient for the fore foil. This case effectively demonstrates the ability of the ShpO to "detune" a component's performance. It highlights the method's versatility in achieving desired performance metrics, whether they require an increase or a decrease in lift, providing designers with a precise tool for load management in complex systems.

Table 4.3: Comparison of final hydrodynamic performance coefficients for optimization cases 8 and 9, at 9° common position angle.

Case	**Description**	$C_{Lcombined}$	$\mathbf{C_{D,\text{total}}}$	$C_{Lcombined}/C_{Dcombined}$
Case 8	Aft foil match the fore lift	2.734	0.0741	33.25
Case 9	Fore foil match the aft lift	2.25	0.0698	34.25

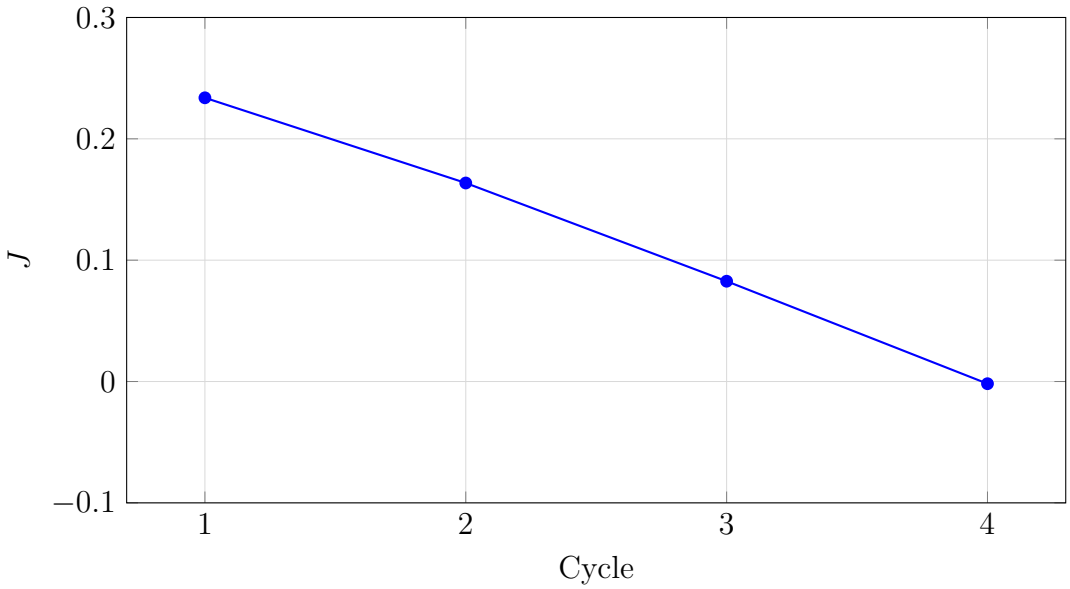

Figure 4.52: Case 9: Evolution of J over 4 optimization cycles.

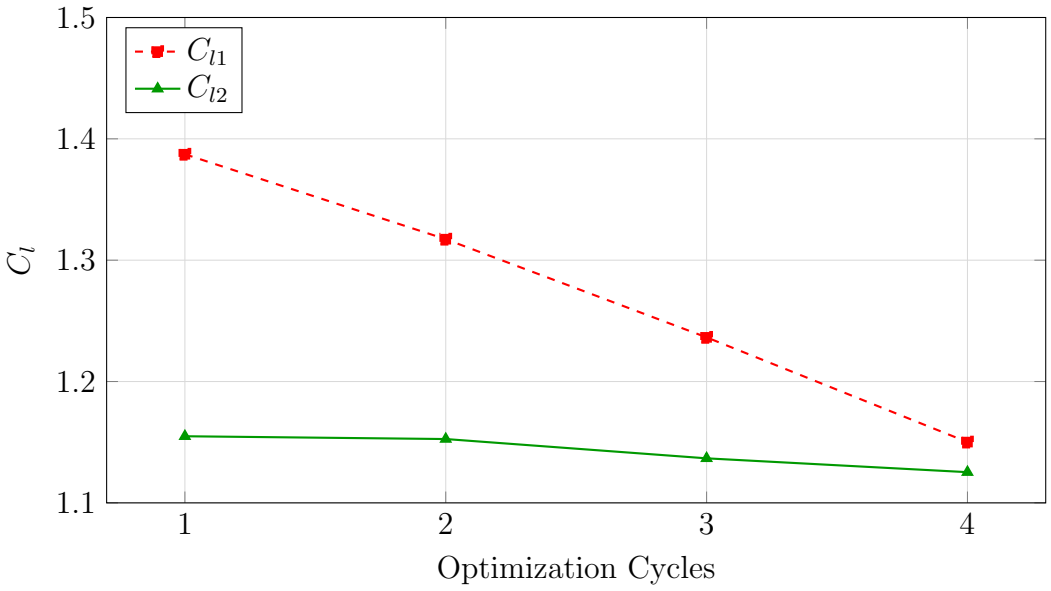

Figure 4.53: Case 9: Evolution of C_{l1} and C_{l2} over 4 optimization cycles.

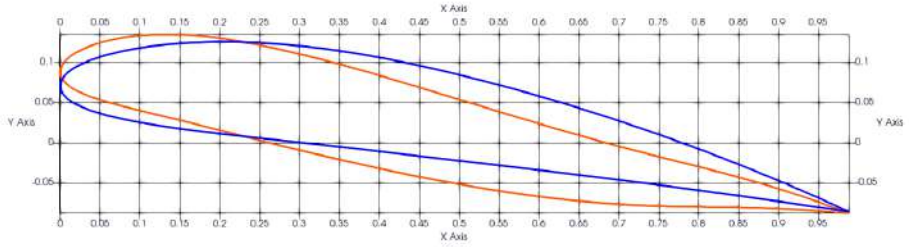

Figure 4.54: Case 9: Geometry before and after optimization at the fore hydrofoil, at 9° common position angle.

Figure 4.55: Case 9: Pressure field around the optimized fore geometry and the original aft hydrofoil, at 9° common position angle.

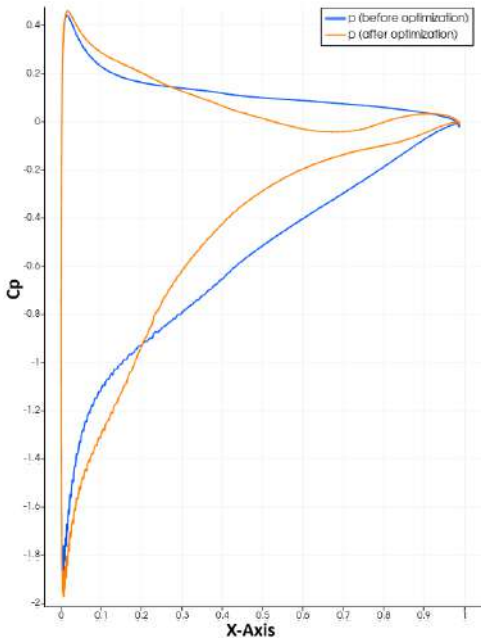

Figure 4.56: Case 9: Pressure distribution before and after the 4 optimization cycles.

Chapter 5

Conclusions

This MSc thesis has presented a comprehensive numerical investigation into the CFD shape optimization of two hydrofoils arranged in a tandem configuration, at the same position angle. The study was conducted using the open-source CFD software OpenFOAM, coupled with the adjointOptimisationFoam library developed by the PCOpt/NTUA, which implements the continuous adjoint method for efficient gradient computation and shape sensitivity analysis.

Case	C_L		C_D		**Combined**	
	$Fore$	Aft	$Fore$	Aft	$C_{L,\,combined}$	$C_{D,\,combined}$
1	1.392	1.422	0.021	0.071	2.81	0.092
2	1.389	1.415	0.020	0.069	2.80	0.090
3	1.613	1.217	0.028	0.064	2.83	0.092
4	1.631	1.183	0.021	0.062	2.81	0.083
5	1.615	1.348	0.021	0.067	2.96	0.085
6	1.634	1.361	0.019	0.068	2.99	0.088
7	1.624	1.361	0.019	0.068	2.99	0.088
8	1.367	1.361	0.014	0.060	2.73	0.074
9	1.150	1.125	0.025	0.046	2.25	0.0698

Table 5.1: Comparison of final hydrodynamic performance coefficients for each optimization case, at 9°common position angle.

The primary objective was to explore the potential performance improvements achievable through ShpO under various operational and design constraints, with a focus on lift maximization and drag minimization. The baseline geometry used was the NACA 4412 hydrofoil, and all simulations

were performed at a Reynolds number of 10^6 and a common position angle of 9°, ensuring fully turbulent flow and significant hydrodynamic interaction between the foils. The computed coefficients of each case are presented in table 5.1.

Key findings and contributions of this work are summarized as follows:

- **Grid independence and computations:** The generated grids were evaluated through grid independence studies and the computation results were presented along with the computed coefficients. They confirmed the accuracy and reliability of the OpenFOAM CFD cases setup for both single and tandem hydrofoil configurations. The use of the k-ω SST turbulence model and detailed mesh refinement levels ensured high-fidelity flow resolution, particularly in the boundary layers and wake regions.

- **Tandem Hydrofoil Interactions:** The parametric study of leading edge-to-edge distance revealed interference effects between the fore and aft hydrofoils. The fore foil experiences an increase in lift due to effective flow acceleration, while the aft foil operates within the wake of the fore foil, resulting in reduced effective inflow velocity and lift.

- **Effectiveness of Adjoint-Based gradients calculation:** The adjoint method proved to be a highly effective tool for gradients computation, utilized in the ShpO which enabled significant performance improvements with moderate computational cost. Across all optimization cases, lift coefficients were increased by up to 25% for the aft foil (case 1) and 16% for the fore foil (case 3), demonstrating the method's capability to tailor hydrofoil shapes for specific objectives.

- **Single target optimization vs. single target with weighted functions optimization:** Case 1 & 4 (lift maximization only) showed that single-objective optimization can lead to improved geometries with massively increased lift. If weighted functions are included in the applied objective formulations (e.g., Cases 2 & 4: lift maximization and drag minimization as weights in the single target), they produce more balanced and physically realistic designs, highlighting the importance of including drag as a constraint or secondary objective in practical applications. Furthermore, optimizing the fore foil proved to be the most effective strategy for single foil optimization (in tandem mode), consistently generating the highest lift-to-drag ratios by favorably conditioning the flow for the entire tandem system and total common forces.

- **Tandem setup common optimization:** Cases 5–7 demonstrated that optimizing both foils together—either on the sensitivities of one or both foils—yielded the best overall system performance. This underscores the importance of a holistic approach to multi-component systems, where interactions between components significantly influence global metrics such as total lift and drag. From all the cases studies, cases 6 and 7 that optimize the fore and both foils respectively at the same time while keeping a common geometry, are obtaining the best lift. At the same time, the aft foil ShpO to case 5 with common geometry at both foils will produce the most balanced results, along with the higher C_L/C_D ratio.
- **Lift Matching and Control:** Cases 8 and 9, as expected, successfully demonstrated the ability to match lift values between fore and aft foils through targeted ShpO. This capability is particularly valuable in any vessel or vehicle design, where balanced load distribution is critical for stability and structural integrity.
- **Practical Relevance:** The optimized hydrofoils exhibited improved lift-to-drag characteristics, which can directly translate into enhanced efficiency for high-speed marine vessels. The ability to customize foil shapes allows designers to better allocate hydrodynamic loads, improve fuel efficiency, and meet specific operational requirements.

In conclusion, this thesis has successfully demonstrated the applicability and effectiveness of the continuous adjoint method for calculating gradients and utilizing them at shpO of tandem hydrofoils.

5.1 Future Work

The present study provides a solid foundation for the shape optimization of tandem hydrofoils, utilizing the adjoint-based method of gradients computation. However, several avenues remain open for further research to enhance the realism, accuracy, and applicability of the findings. Future work can be extended in the following directions:

- **Free Surface Effects:** A critical extension would be to model the interaction with a free surface.
- **Different Position Angles Between Hydrofoils:** A comprehensive parametric study where the angle of attack of the fore and aft foils is varied independently would be highly valuable.

- **Study of Different Vertical Heights (Stagger):** Introducing a vertical offset (stagger) between the hydrofoils would allow the aft foil to operate either in the downwash or upwash of the fore foil, significantly altering the inflow conditions.
- **Evaluation at Different Reynolds Numbers:** Conducting studies across a range of Reynolds numbers would assess the scalability and robustness of the optimized designs.
- **Applying Multiple Objective Optimization and Pareto generation:** Conducting studies with MOO of various targets (e.g. lift, drag, area) and generating Pareto charts based on the results.

Bibliography

[1] Faltinsen, O. M. (2005). Hydrodynamics of High-Speed Marine Vehicles. Cambridge University Press.

[2] https://en.wikipedia.org/wiki/Raketa_(hydrofoil)

[3] Akhtar, I., Mittal, S. (2005). A computational study of the flow around tandem airfoils. In 43rd AIAA Aerospace Sciences Meeting and Exhibit (p. 1265).

[4] Ducoin, A., Young, Y. L., Astolfi, J. A. (2012). An experimental and numerical study of a hydrofoil at cavitating conditions. Journal of Fluid Mechanics, 706, 295-343.

[5] https://www.messynessychic.com/2016/04/20/river-rockets-of-the-soviet-space-age/

[6] Zheng, Z., Wang, K., Yang, W. (2020). Numerical investigation of the interference effects between tandem hydrofoils with a wide spacing range. Ocean Engineering, 217, 107992.

[7] Young, Y. L., Savander, B. R. (2011). Performance-based design and optimization of deformable hydrofoils. Journal of Fluids and Structures, 27(5-6), 788-800.

[8] Giannakoglou, K. C. (2011). Methods of Deterministic and Stochastic Optimization and Applications, Notes for the Postgraduate Course (MSc Program), Athens.

[9] J. Nocedal and S.J. Wright. Numerical Optimization. Springer, New York, 1999

[10] Giannakoglou, K. C. (2006). Optimization Methods in Aerodynamics (4th ed., with exercises). Athens

[11] https://www.openfoam.com/

[12] ttps://www.openfoam.com/documentation/guides/v2112/doc/guide-mesing-blockmesh.html

[13] ttps://www.openfoam.com/documentation/guides/latest/doc/guide-mesing-snappyhexmesh.html

[14] USER MANUAL "adjointOptimisationFoam, an OpenFOAM-based optimisation tool", 2023.

[15] Menter, F. R., "Two-Equation Eddy-Viscosity Turbulence Models for Engineering Applications," AIAA Journal, Vol. 32, No. 8, August 1994.

[16] ttps://turbmodels.larc.nasa.gov/sst.tml.

[17] E.M. Papoutsis Kiachagias, N. Magoulas, J. Mueller, C. Othmer, and K.C. Giannakoglou. Noise reduction in car aerodynamics using a surrogate objective function and the continuous adjoint method with wall functions. Computers & Fluids, 2015.

[18] I.S. Kavvadias, E.M. Papoutsis-Kiachagias, G. Dimitrakopoulos, and K.C. Giannakoglou. The continuous adjoint approach to the k–omega SST turbulence model with applications in shape optimization.

[19] E.M. Papoutsis-Kiachagias. Adjoint Methods for Turbulent Flows, Applied to Shape or Topology Optimization and Robust Design. PhD thesis, National Technical University of Athens, 2013.

[20] L. Piegl and W. Tiller. The NURBS book. Springer, 1997.

[21] https://web.mit.edu/drela/Public/web/xfoil/

[22] Smith, A. M. O. (1975). High-Lift Aerodynamics. Journal of Aircraft, 12(6), 501-530.

[23] Bratton, P., Collie, S. (2021). Review of Tandem Foil and Wing Systems for Performance Enhancement. Progress in Aerospace Sciences, 125, 100726.